

# An Atomic Cluster Expansion Potential for Twisted Multilayer Graphene

Yangshuai Wang,<sup>1,\*</sup> Drake Clark,<sup>2,†</sup> Sambit Das,<sup>3,‡</sup> Ziyang Zhu,<sup>4,5,§</sup> Daniel Massatt,<sup>6,¶</sup> Vikram Gavini,<sup>7,\*\*</sup> Mitchell Luskin,<sup>2,††</sup> and Christoph Ortner<sup>8,‡‡</sup>

<sup>1</sup>*Department of Mathematics, National University of Singapore, 10 Lower Kent Ridge Road, Singapore 119076.*

<sup>2</sup>*School of Mathematics, University of Minnesota, Minnesota, USA 55455.*

<sup>3</sup>*Department of Mechanical Engineering, University of Michigan, Ann Arbor, Michigan, USA 48109*

<sup>4</sup>*Stanford Institute for Materials and Energy Sciences,*

*SLAC National Accelerator Laboratory, 2575 Sand Hill Road, Menlo Park, CA 94025, USA*

<sup>5</sup>*Department of Physics, Boston College, Chestnut Hill, MA 02467, USA*

<sup>6</sup>*Department of Mathematics, Louisiana State University, USA 70803*

<sup>7</sup>*Department of Mechanical Engineering, Department of Materials Science & Engineering, University of Michigan, Ann Arbor, Michigan, USA 48109*

<sup>8</sup>*Department of Mathematics, University of British Columbia, 1984 Mathematics Road, Vancouver, BC, Canada V6T 1Z2.*

(Dated: June 19, 2025)

Twisted multilayer graphene, characterized by its moiré patterns arising from inter-layer rotational misalignment, serves as a rich platform for exploring quantum phenomena. While first-principles calculations are computationally prohibitive and empirical interatomic potentials often lack accuracy, machine-learning interatomic potentials (MLIPs) present a promising alternative, offering (near-)DFT accuracy at a significantly reduced computational cost. Despite their success in two-dimensional monolayer materials, MLIPs remain under-explored in twisted multilayer graphene systems. In this work, we develop an Atomic Cluster Expansion (ACE) potential for simulating twisted multilayer graphene and test it on a range of simulation tasks. We propose an approach to construct training and test datasets that incorporate all possible twist angles and local stacking, including incommensurate ones. To achieve this, we generate configurations with periodic boundary conditions suitable for DFT calculations, and then introduce an internal twist and shift within those supercell structures. We further refine the dataset through active learning filtering, guided by Bayesian uncertainty quantification. Our model is validated for accuracy and robustness through a wide range of numerical tests.

## I. INTRODUCTION

Multilayer graphene has garnered significant attention due to its unique electronic properties and potential applications in next-generation devices [1, 2]. When graphene layers are stacked with a slight rotational misalignment, known as a twist angle, they form moiré patterns, leading to novel physical phenomena [3–6]. Understanding these phenomena is crucial for advancing condensed matter physics and developing materials with tunable electronic characteristics. The ability to manipulate these properties through the twist angle makes the twisted graphene systems a versatile platform for exploring quantum mechanical effects. Consequently, research into twisted bilayer and multilayer graphene holds great promise for innovations in nanoelectronics, photonics, and quantum computing.

First-principles calculations of material properties offer a robust method for discovering new materials and optimizing existing ones. However, these calculations are resource-intensive and their applicability is often limited. This limitation is especially pronounced in multilayer twisted materials, which do not always conform to periodic boundary conditions, rendering first-principles methods such as density functional theory (DFT) computationally infeasible. Empirical interatomic potentials (IPs), including Lennard-Jones [7], the embedded atom method (EAM) [8], Stillinger-Weber [9], and Kolmogorov-Crespi [10, 11] provide significant computational speed-ups—typically by six to eight orders of magnitude compared to DFT. These potentials, with their straightforward and physically motivated forms, offer reasonable predictions for low-energy structures but generally fall short in achieving the quantitative accuracy of DFT, particularly when reproducing macroscopic properties.

To overcome these limitations, machine-learning interatomic potentials (MLIPs) have emerged as a transformative approach in molecular and materials simulation [12–16]. MLIPs enable the simulation of atomistic systems at or

\* yswang@nus.edu.sg

† clar1939@umn.edu

‡ dsambit@umich.edu

§ ziyang.zhu@bc.edu

¶ dmassatt@lsu.edu

\*\* vikramg@umich.edu

†† luskin@umn.edu

‡‡ ortner@math.ubc.ca

near the accuracy of electronic structure methods while being computationally cheaper by orders of magnitude. This capability has made the simulation of large-scale systems and long time-scales at high accuracy accessible, establishing MLIPs as indispensable tools for atomic-scale simulation. Recent comprehensive reviews of the field are provided in [17–20]. Of particular relevance to the present work are the atomic cluster expansion and related methods introduced in [13–16]. The creation of an MLIP begins with a flexible functional form, constrained only by physical requirements in which there is high confidence, for example, to comply with the natural symmetries of the potential energy in three-dimensional space. Parameters are then estimated using reference data, typically energies, forces, and virial stresses from a representative set of atomic configurations. This data is usually generated via quantum mechanical techniques, such as DFT calculations, which are often limited to relatively small structures. A well-trained MLIP is expected to provide accurate predictions for processes on both similar and much larger spatial scales.

The Atomic Cluster Expansion (ACE), introduced in [16], is a particularly flexible and theoretically sound MLIP approach. ACE offers a balance between cost and accuracy and has been successfully applied across a wide range of tasks, particularly in materials simulation [21–28]. Linear variants of the ACE model have proven to be both data and computationally efficient, making them particularly useful in active learning (AL) workflows [25]. Linearity also facilitates sensitivity analysis and paves the way for reliable uncertainty quantification. Throughout this work, we adopt the ACE method, but the methods and benchmarks we introduce are likely applicable to the vast majority of MLIPs frameworks.

Although MLIPs have been extensively utilized in various fields, their application to twisted multilayer graphene systems remains largely unexplored. Previous studies have developed MLIPs for other two-dimensional (2D) materials, such as MoS<sub>2</sub>, monolayer graphene, buckled silicone, and quaternary transition metal dichalcogenide (TMD) alloy, to investigate thermal conductivity and phononic properties [29–33]. For instance, Magorrian *et al.* [34] focused on atomistic relaxation in twisted bilayers of InSe, while Jung *et al.* [35] explored mechanical and fracture dynamics in monolayer graphene. Yin *et al.* [36] applied machine-learning force fields for membrane design, and Wilson *et al.* [37] used batch active learning to construct MLIPs, emphasizing phonon dispersion and phase transition temperature calculations for monolayer GeSe. More recently, Bao *et al.* [38] leveraged transfer learning to predict the electronic structure of twisted MoTe<sub>2</sub>, while a closely related study [39] developed a framework for constructing MLIPs for moiré systems, specifically MX<sub>2</sub> (M = Mo, W; X = S, Se, Te) materials. Georgaras *et al.* [40] further advanced this direction by proposing a split MLIP architecture and a curated dataset strategy that explicitly distinguishes intralayer and interlayer interactions, leading to improved accuracy in modeling moiré materials. However, these studies primarily focus on relatively simple physical properties such as relaxed lattice constants, phonon spectra, and band structures. To the best of our knowledge, no MLIP has been specifically developed for twisted multilayer graphene systems, nor has there been a comprehensive benchmark of such systems, which serves as the primary motivation for our work.

In this study, we develop a training and benchmark protocol for twisted multilayer graphene systems and apply it to fitting an ACE model. A key challenge in developing an MLIP is the selection of small-scale training structures. For twisted multilayer graphene this is particularly challenging since most twist angles of interest cannot be represented in a small periodic structure accessible to DFT methods. A novel contribution of our work to overcome this is to employ locally twisted training structures. This provides a systematic method to generate training configurations with periodic boundary conditions that are suitable for DFT calculations across all twist angles. We combine this approach with Bayesian active learning and filtering techniques that sub-select configurations based on uncertainties derived from Bayesian linear regression.

Our evaluation of the developed models includes several numerical experiments designed to test the effectiveness of our method compared with naively generated datasets, as well as the in-distribution accuracy and out-of-distribution robustness of the resulting fitted models. Our tests include geometry optimization, focusing on defect formation and migration within the twisted layers, molecular dynamics (MD) simulations including static, dynamic, and thermodynamic limits. These simulations provided insights into the material’s stability, response to thermal fluctuations, and overall dynamical behavior. Additionally, we performed phonon calculations to explore the vibrational properties of twisted multilayer graphene, which is crucial for understanding its thermal conductivity and other phonon-related phenomena. Our tests demonstrate the wide applicability and effectiveness of our approach to training MLIPs for twisted multi-layer structures.

## II. METHODS

### A. Multilayer twisted graphene

We focus on multilayer twisted graphene, but the methodologies we develop for this case are readily extendable to other layered 2D materials. A single layer of graphene has a honeycomb structure (see Figure 1 left) associated with

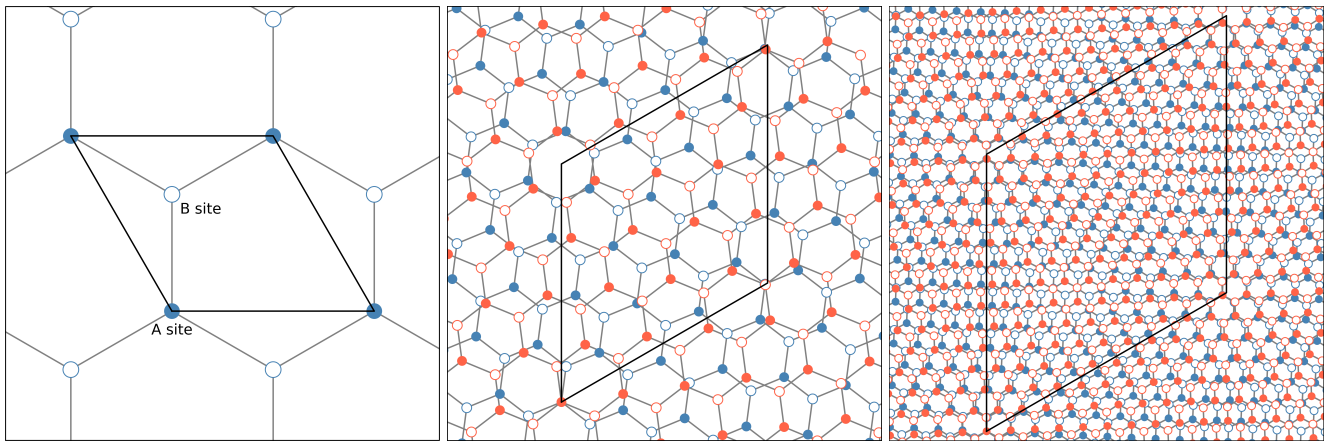


FIG. 1: Graphene unit cell (left); moiré cell for 15° twisted bilayer graphene (center); moiré cell for 5° twisted bilayer graphene (right).

a lattice whose fundamental matrix is

$$A = a_0 \begin{pmatrix} 1 & -1/2 \\ 0 & \sqrt{3}/2 \end{pmatrix}. \quad (1)$$

Each unit cell of graphene has two carbon atoms with shifts  $b_A = (0, 0)^T$  and  $b_B = a_0(0, \sqrt{3}/3)^T$ , labeled “A site” and “B site” in Figure 1. For our numerical results we used the lattice constant  $a_0 = 2.47$  Å. Twisted bilayer graphene is formed by stacking two layers of graphene on top of each other with a relative twist. The two layers’ fundamental matrices are then:

$$A_1 = R_{-\theta/2}A, \quad A_2 = R_{\theta/2}A, \quad \text{with } R_\phi = \begin{pmatrix} \cos \phi & -\sin \phi \\ \sin \phi & \cos \phi \end{pmatrix}. \quad (2)$$

The misalignment between the two layers caused by the twist angle produces a large-scale moiré pattern. The resulting bilayer structure is generally incommensurate and only exhibits approximate periodicity. Exact periodicity is achieved only at specific twist angles where  $\cos \theta$  satisfies a Diophantine condition [41, 42]. The moiré unit cell has the form [43–45]:

$$A_M := (A_1^{-1} - A_2^{-1})^{-1}, \quad A_M(\theta) = \frac{a_0}{2 \sin(\theta/2)} \begin{pmatrix} 0 & \frac{\sqrt{3}}{2} \\ -1 & \frac{1}{2} \end{pmatrix}. \quad (3)$$

The moiré superlattice length depends on the rotation angle between two layers  $\theta$ , growing as  $\sim 1/\theta$  as  $\theta$  decreases. Techniques that rely on periodic boundary conditions or supercell approximations require impractically large domains for numerical purposes. This effect is even more severe in the multi-layer case [46, 47].

The large length scale of moiré patterns and lack of periodicity make numerical simulation of many interesting phenomena in the small-angle regime challenging. A wide variety of strongly correlated electronic phases of matter such as superconductivity [48] and fractional quantum anomalous Hall (fQAH) states [49, 50] can emerge. Mechanical properties, which are the primary focus of the present paper, including structural relaxation [5, 44, 45, 47, 51–54], phonons [55–57], and defects [58, 59], play a critical role in understanding the electronic behavior of these moiré systems. For example, mechanical relaxation can form large triangular or hexagonal domains [60], modifying electronic structures and shifting the twist angle at which fQAH is expected to appear. Additionally, strong electron-phonon coupling, which has been measured [61], may contribute to the observed moiré superconductivity. Defects are also prevalent in these moiré systems and their impact on electronic properties is not yet understood.

Mechanical relaxation of multilayer graphene systems has in the past been performed using linear elasticity approximations or the REBO interatomic potential for the intralayer component and the generalized stacking fault energy or the Kolmogorov-Crespi interatomic potential [10] for the interlayer component [44, 45, 47, 51, 52, 62]. Although the Kolmogorov-Crespi interatomic potential [10] is a major improvement over two-body interatomic potentials such as Lennard-Jones, there are significant errors in the prediction of forces of some important local configurations (disregistries) when compared to DFT computations [63]. An important perspective of our present work is to develop a methodology (in the simplified multi-layer graphene setting) that can be readily extended to systematically construct accurate interatomic potentials for more complex 2D materials such as the transition metal dichalcogenides (TMDs).

## B. The linear ACE framework

Accurate energy and force calculations are best achieved through electronic structure techniques such as DFT. However, DFT has limitations due to computational cost for large systems and long timescales. To overcome these limitations, MLIPs, trained on DFT data, have become essential in computational materials science due to their high accuracy and transferability, but relatively low computational cost [17–20].

We utilize the linear atomic cluster expansion (ACE) parametrization [16, 22, 64]. MLIPs for materials typically express the total energy as a sum over individual site energies. To that end, we consider  $N$  atoms described by their position vectors  $\mathbf{r}_j$ . A set  $\mathbf{A} := \{\mathbf{r}_1, \dots, \mathbf{r}_N\} \in \mathbb{R}^{3N}$  of  $N$  particle positions is called an atomic configuration. We suppress the specification of a unit cell and periodicity for the sake of simplicity of presentation. One normally also accounts for the chemical elements, but since this work is only concerned with models for multi-layer graphene, we can ignore this dependency as well.

Let  $\mathbf{r}_{ij} = \mathbf{r}_j - \mathbf{r}_i \in \mathbb{R}^3$  be the relative position vector between atom  $j$  and a reference atom  $i$  and  $r_{ij} = |\mathbf{r}_{ij}|$  the distance. Given a cutoff radius  $r_{\text{cut}}$  (the first model hyperparameter), we define the *local* atomic environment as  $\mathbf{A}_i := \{\mathbf{r}_{ij}\}_{r_{ij} \leq r_{\text{cut}}}$ .

The total energy of a structure of this kind is decomposed into dispersion interaction and short-ranged many-body site energies

$$E(\mathbf{A}; \mathbf{c}) = E_{\text{disp}}(\mathbf{A}) + \sum_{i=1}^N \varepsilon(\mathbf{A}_i; \mathbf{c}), \quad (4)$$

where the dispersion interaction  $E_{\text{disp}}$  will always be the D3 dispersion model [65] and the site energy  $\varepsilon$  is a “learnable” function of an atomic environment  $\mathbf{A}_i$ . It’s parameters  $\mathbf{c}$  will be determined through regression. While the vast majority of local MLIPs are written in the form (4), the ACE model we employ has the additional feature that each site energy is explicitly expanded into many-body terms,

$$\varepsilon(\mathbf{A}_i; \mathbf{c}) = \sum_{\nu=0}^{\nu_{\text{max}}} \frac{1}{\nu!} \sum_{j_1, \dots, j_\nu} V_\nu(\mathbf{r}_{ij_1}, \dots, \mathbf{r}_{ij_\nu}; \mathbf{c}). \quad (5)$$

The repeated indices in the summation are deliberate and result in a highly computationally efficient implementation (cf. Appendix A). After further expanding each potential  $V_\nu$  in a basis, the ACE site energy  $\varepsilon$  can then finally be expressed as

$$\varepsilon(\mathbf{A}_i; \mathbf{c}) := \mathbf{c} \cdot \mathcal{B}(\mathbf{A}_i) = \sum_{B \in \mathcal{B}} c_B B(\mathbf{A}_i), \quad (6)$$

with basis functions  $B$  and parameters  $\mathbf{c} := \{c_B\}_{B \in \mathcal{B}}$  that are optimized via linear least squares (cf. (7)).

Both total energy  $E$  and site energy  $\varepsilon$  must be invariant under permutations, rotations, and reflections of the inputs; hence the basis  $\mathcal{B}$  is constructed to satisfy the same invariance exactly. In addition, the basis functions inherit the natural ordering of (5), providing a physically interpretable hyper-parameter  $\nu_{\text{max}}$  to converge the fit accuracy. A more detailed review of the ACE model and its (hyper-)parameters is given in Appendix A.

To estimate the model parameters  $\mathbf{c}$  we require a training dataset which contains a list of atomic configurations  $\mathfrak{A} = \{\mathbf{A}\}$  and corresponding observations evaluated using reference electronic structure models (we employ DFT; cf. Appendix C for details). For each configuration  $\mathbf{A}$ , the total energy  $E^{\text{ref}}(\mathbf{A}) \in \mathbb{R}$ , forces (negative energy gradient)  $F^{\text{ref}} := -\nabla E^{\text{ref}}(\mathbf{A}) \in \mathbb{R}^{N \times 3}$  (where  $N$  is the total number of atoms in each configuration  $\mathbf{A}$ ) and virial stress  $\Sigma^{\text{ref}}(\mathbf{A}) \in \mathbb{R}^{3 \times 3}$  are included. We use a regularized linear least squares method to estimate the parameters, requiring minimization of the quadratic loss function:

$$\begin{aligned} \mathcal{L}(\mathbf{c}) := & \sum_{\mathbf{A} \in \mathfrak{A}} \left( N_{\mathbf{A}}^{-1} w_E^2 |E(\mathbf{A}; \mathbf{c}) - E^{\text{ref}}(\mathbf{A})|^2 + w_F^2 |F(\mathbf{A}; \mathbf{c}) - F^{\text{ref}}(\mathbf{A})|^2 \right. \\ & \left. + N_{\mathbf{A}}^{-1} w_\Sigma^2 |\Sigma(\mathbf{A}; \mathbf{c}) - \Sigma^{\text{ref}}(\mathbf{A})|^2 \right) + \lambda \|\Gamma \mathbf{c}\|^2, \end{aligned} \quad (7)$$

where  $N_{\mathbf{A}}$  is the number of atoms in structure  $\mathbf{A}$ ,  $F(\mathbf{A}; \mathbf{c})$  is a vector of forces,  $\Sigma(\mathbf{A}; \mathbf{c})$  is the virial stress of the ACE model,  $\Gamma$  specifies the form of the regularizer (smoothness prior), and  $\lambda$  is a scaling parameter that determines the relative weight of regularization. The weights  $w_E$ ,  $w_F$  and  $w_\Sigma$  adjust the contributions of energy, forces and virial stresses, respectively. Within the Bayesian interpretation of ridge regression (also used as the solver, see the discussion below),  $\Gamma$  defines a prior distribution for the model parameters  $\mathbf{c} \sim \mathcal{N}(\mathbf{0}, \Gamma^{-2})$ . For details, see Appendix B and [64]. Throughout the present work, we choose an algebraic smoothness prior of strength  $p = 5$ , as defined in [64, Eq.10].

Due to the linearity of the ACE model (6), minimizing the quadratic loss (7) is equivalent to solving a linear least squares problem. Various solvers are available for this task; see [64] for an overview and benchmark tests. In this work, we employ Bayesian linear regression to solve the problem, as it automatically selects the regularization parameter  $\lambda$  and produces a *posterior* parameter distribution that we can then employ for uncertainty quantification. We briefly review the approach with detailed discussions deferred to Appendix B.

By assuming an isotropic Gaussian prior on the model parameters and Gaussian independent and identically distributed (i.i.d) noise on observations, we obtain an explicit posterior distribution  $\text{post}(\mathbf{c})$  for the parameters, from which the standard deviation of the posterior-predictive distribution of total energies (and other quantities) can be deduced. Using the posterior directly is computationally expensive for a large basis; scaling as  $O(N_{\text{basis}}^2)$ , hence we generate an ensemble of parameters  $\{\mathbf{c}^k\}_{k=1}^K$  obtained by sampling from the posterior  $\text{post}(\mathbf{c})$ , where  $K$  is the number of sample (or, committee size). Each parameter vector  $\mathbf{c}^k$  results in predicted energies  $E^k$  (as well as forces, virials, etc). (See Appendix B and [25, 64] for further details.) This results in an energy uncertainty estimate

$$\sigma^E := \sqrt{\frac{1}{\beta w_E^2} + \frac{1}{K} \sum_{k=1}^K (E^k - \bar{E})^2}, \quad (8)$$

where  $\beta$  is a hyperparameter (see Appendix B for details),  $\bar{E} := \sum_{i=1}^N \sum_{B \in \mathcal{B}} \bar{c}_B \cdot B(\mathbf{A}_i)$  with  $\bar{\mathbf{c}}$  being the posterior mean of the distribution and  $E^k$  denoting the total ACE energy evaluated using  $\mathbf{c}^k$ . This approach is computationally efficient, requiring only a single basis evaluation followed by  $K$  dot products with the ensemble parameters. Similarly, the corresponding relative force uncertainty for the  $i$ -th atom, as defined in [25], is given by:

$$\sigma_i^F := \frac{1}{K} \sum_{k=1}^K \frac{\|F_i^k - \bar{F}_i\|}{\|\bar{F}_i\| + \varepsilon}, \quad (9)$$

where  $\bar{F}_i$  is the mean force prediction for the  $i$ -th atom, and  $\varepsilon$  is a regularization constant to prevent divergence, set to 0.2 eV/Å. In the following section, we use  $\max_i \sigma_i^F$ , the maximum force uncertainty among all atoms in a given configuration, as the criterion for selecting a candidate dataset that is as small as possible while still accurately capturing the properties of interest.

### C. Dataset generation

In this section, we describe the process of generating the training and test datasets used to fit and validate the potentials employed in benchmarking twisted multilayer graphene.

#### 1. Locally twisted multi-layers

As mentioned in § II A, bilayer graphene systems with twist angle  $\theta$  are only periodic for specific values of  $\theta$ . We used periodic supercells with twist angles  $\theta = \phi_2 - \phi_1$  for  $\phi_1$  and  $\phi_2$  satisfying

$$\cos(\phi_1) = \frac{p+2q}{2n}, \quad \cos(\phi_2) = \frac{2p+q}{2n}, \quad (10)$$

where  $p, q, n$  are integers satisfying the Diophantine equation [41]

$$p^2 + q^2 + p \cdot n = n^2. \quad (11)$$

The seven smallest such commensurate systems and their supercell atom count are given in [41, Table II]. These supercells quickly become intractable for DFT computations as the angle gets smaller. There is a more general Diophantine equation that can be solved to form commensurate cells [42], but these still suffer from the same size issue.

To train beyond this limitation, we introduce a “local twisting procedure.” We first introduce the procedure for bilayers and then generalize it to multilayers. Let the origin be the center of a commensurate supercell with twist angle  $\theta_{\text{sc}}$ . Pick two circles inscribed in the supercell with radii  $r_1 < r_2$  (see Figure 2). Then we transform the  $j^{\text{th}}$  layer’s positions by

$$\Lambda_j(x) := R[\Phi(|x|; (-1)^j(\theta - \theta_{\text{sc}})/2)]x + b_j$$

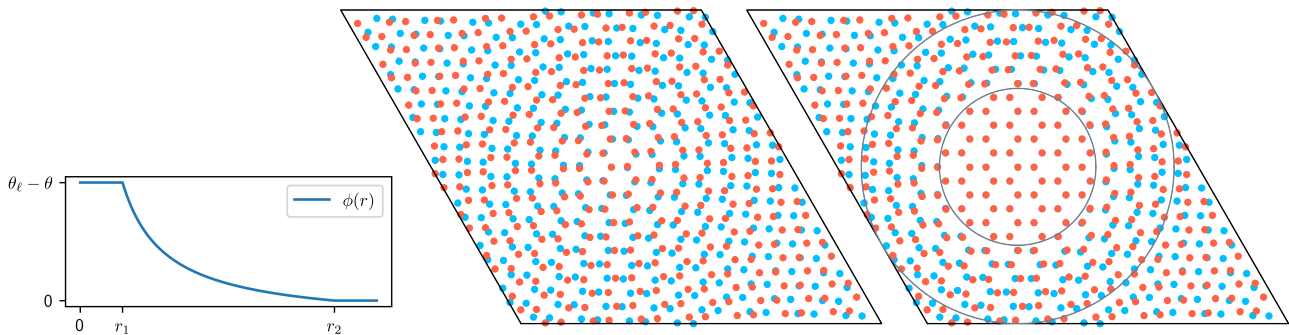


FIG. 2: Left: Angle blending function  $\Phi(r)$ ; Center: Commensurate Supercell of bilayer for  $\theta_{sc} = 4.41^\circ$  (676 atoms); Right: Local twisting to  $\theta = 0^\circ$ .

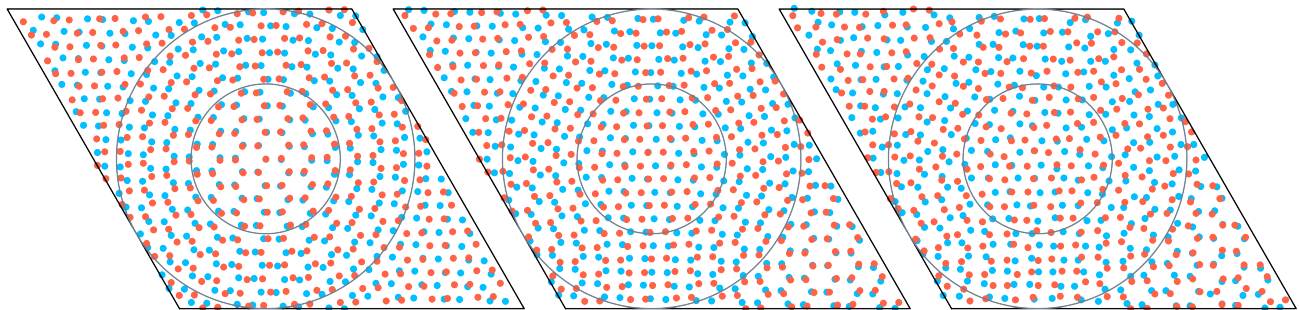


FIG. 3: Left: Local twisting to  $\theta = 3.0^\circ$ ; Center: Disregistry shifting center to AB; Right: Random (normal) perturbation with stdev 0.07 times AB distance.

where  $R[\phi]$  is a rotation through angle  $\phi$ ,  $b_j$  is the global disregistry shift of layer  $j$ , and  $\Phi$  is an empirically chosen angle blending function given by

$$\Phi(r; \phi) = \begin{cases} \phi, & \text{if } r < r_1, \\ \phi \frac{r_1 r_2}{r_2 - r_1} \left( \frac{1}{r} - \frac{1}{r_2} \right), & r \in (r_1, r_2), \\ 0, & r > r_2; \end{cases}$$

see Figure 2 and Figure 3 for examples including twists and shifts. The rotation by  $\Phi$  untwists locally by half the collective supercell angle per layer, and rotates by half the desired local twist.

Near the origin the geometry exactly corresponds to a twisted bilayer with relative shift  $b = b_1 - b_2$  and twist angle  $\theta$ , but the system globally maintains periodicity and slow variation of the displacement field. The two parameters  $b, \theta$  can be chosen arbitrarily; that is, in principle this procedure is capable of generating structures that contain all possible twist angles and shifts.

The procedure described in the foregoing paragraph can be extended to three or more alternating supercell layers. The main restriction remains the periodicity of every layer on the chosen supercell limiting the choices of global twist angles between layers. Here, we employ alternating twist angles where all adjacent layers are twisted relative to each other by alternating  $\theta_{sc}$  or  $-\theta_{sc}$ , where  $\theta_{sc}$  is the commensurate twist angle corresponding to the supercell. Let the origin again be the center of the commensurate supercell. In this case of alternating twist, we apply a similar deformation map

$$\Lambda_j(x) := R[\Phi(|x|; \theta_j)]x + b_j$$

where  $b_j$  is the local shift of layer  $j$  and  $\theta_j$  is the relative rotation from the supercell angle, and the twist between layer  $j$  and layer  $j + 1$  is given by  $\theta_{j+1} - \theta_j + (-1)^j \theta_{sc}$ .

## 2. Filtering the candidate dataset

To use the uncertainty introduced in Section II B for selecting representative configurations, we first need to construct a candidate dataset. The dataset includes monolayer, bilayer and trilayer graphene systems, with quadrilayer and pentalayer configurations reserved for out-of-distribution generalization testing (cf. Table II). The dataset is constructed as follows: For a single layer of graphene, we took the graphene structure discussed in Section II A and considered  $n \times n$  unit cells where  $n$  ranges from 1 to 4. For each of these configurations, we then picked an amplitude and randomly perturbed each atom’s position with a normal distribution with an average of 0 and with a standard deviation equal to this amplitude. We do this for a thousand different amplitudes evenly spaced between 0 and 0.15 times the distance between an A and B site of graphene, yielding 4000 single-layer data points to choose from.

For bilayer graphene, we make use of the local twisting method described in Section II C 1. This method allows us to sample over arbitrary local twist angles and a selection of global twist angles (commensurate angles). We generated datasets using global twists of  $16.4^\circ$ ,  $4.41^\circ$ , and  $0^\circ$  (untwisted supercell). For the untwisted case, we used a  $7 \times 7$  supercell. For local twist angles, we chose 25 angles evenly distributed between 0 and  $30^\circ$ . For each local angle we used the closest global twist angle as the surrounding supercell, then performed the local twist method. We dynamically chose the disregistries used for each local twist angle to sample disregistries uniformly for each of the 25 twist angles to scale with the size of the moiré cell (inversely proportional to twist angle). The details of this process are in Appendix D. We used a total of 479 different disregistries across 25 local twist angles.

The trilayer, quadrilayer and pentalayer systems were also all generated using the local twisting method. The commensurate twist angles used were the same as in the bilayer case (no twist,  $4.41^\circ$ ,  $16.4^\circ$ ). Since any comprehensive sampling of the alternating trilayer, quadrilayer and pentalayer would yield too large of a dataset, we randomly selected disregistries, interlayer distances and local twist angle differences. We obtained 500 unrattled and 500 rattled (randomly perturbed) samples for the trilayer, quadrilayer and pentalayer datasets. The disregistries were randomly selected uniformly over the unit cell. The interlayer distances were uniformly sampled between  $2.7 \text{ \AA}$  and  $4 \text{ \AA}$  independently for each pair of layers. The local twist angle differences ( $\theta_j$ ’s from the local twisting method) were uniformly chosen between  $-15^\circ$  and  $15^\circ$ . For the rattled samples, the rattling standard of deviation was selected uniformly from 0 to 0.15 times the AB distance. We could have additionally exploited the symmetries when all layers are rotated or shifted together, however, the hyperactive learning process will bias sampling away from these symmetry directions regardless.

After constructing a large initial candidate dataset, we then design a filtering strategy using the relative force uncertainty  $\sigma_i^F$  defined in (9) to reduce redundancy while maintaining accuracy. The correlation between  $\sigma_i^F$  and true relative force errors, as demonstrated in [25], supports its effectiveness in identifying key configurations. The filtering strategy uses the following “greedy” approach:

1. Choose ACE hyperparameters: Correlation order  $\nu_{\max} = 4$  (body-order five); Polynomial total degree 20; Cutoff radius  $r_{\text{cut}} = 5.5 \text{ \AA}$ ; regression weights  $w_E/w_F/w_V = 10.0/1.0/1.0$ ; Committee size  $K = 20$ . The resulting model has approximately 5k parameters.
2. Begin with an initial dataset of 10 randomly selected configurations from the candidate set.
3. Estimate the model parameters  $\mathbf{c}$  from the current training dataset.
4. Compute the force uncertainties  $\max_i \sigma_i^F$  for all remaining candidate training structures. Add the 50 configurations with the highest force uncertainties to the training set.
5. Repeat from Step 3 until the maximum force uncertainty,  $\max_i \sigma_i^F$ , is reduced to a specified threshold of  $20 \text{ meV/\AA}$ .

This filtering strategy effectively reduced the dataset to approximately 5% of the original candidates while achieving strong generalization between training and testing errors, as we demonstrate in the next section.

## 3. Fine-tuning

It is all but impossible to fit an MLIP that has good quantitative accuracy across all possible simulation tasks for a given material. The models we report will be shown to have excellent accuracy in-distribution (near the training set) and behave robustly with good qualitative accuracy out-of-distribution. In order to obtain quantitatively accurate result on new simulation tasks, it may be necessary to extend the training data in a way that is representative of the new tasks, or within an active learning procedure. Given the low cost of fitting a linear ACE potential it is straightforward to then simply refit the model to the expanded dataset, normally with the same hyperparameters. We will demonstrate this on a limited set of out-of-distribution tests. We call this procedure “fine-tuning” to indicate the analogy with fine-tuning foundation models [66].

Label	Description	Application
ACE (*)	Fitted to dataset as described in Section II C, (0.5k structures, 154k atoms)	Throughout the paper
ACE (gl) ACE (lt) ACE (gt)	Randomly selected configurations from candidate dataset. - Globally and locally twisted (gl), (0.3k struct., 225k atoms) - Locally twisted (lt), (0.3k struct., 203k atoms) - Globally twisted (gt), (0.3k structures, 240k atoms)	Section III B: Geometry optimization
ACE (mo) ACE (bi)	Randomly selected configurations from candidate dataset: - Only monolayer (mo), (0.9k structures, 64k atoms) - Only bilayer (bi), (0.4k structures, 270k atoms)	Section III A: Fitting accuracy Section III C: Molecular Dynamics
KC pacemaker	Comparison interatomic potential models: - Kolmogorov-Crespi potential [10] - Nonlinear ACE potential for general carbon systems [28], (17k structures, 366k atoms)	Section III A: Fitting accuracy; Section III B: Geometry optimization; Section III D: Phonon spectra.

TABLE I: List of potentials tests throughout Section III, including several variants of our linear ACE potential and two comparison potentials from the literature. The reported number of structures and total number of atoms across all structures specifies the amount of data from which the models are trained.

### III. RESULTS

We evaluate the robustness and transferability of the fitted ACE potential trained using the methods introduced in the previous section. We conduct comprehensive numerical tests on twisted graphene at various angles and layer configurations. Section III A assesses the force accuracy of the ACE model. Section III B examines the geometry optimization of graphene configurations to evaluate their static mechanical properties. Section III C presents the performance of the ACE potential in molecular dynamics simulations, demonstrating its capability to compute both static and dynamic properties of twisted bilayer graphene. Section III D investigates the accuracy of phonon spectra.

To compare and demonstrate the effectiveness of training on locally twisted training structures as well as our dataset filtering strategies, we trained various potentials using different dataset constructions. Table I summarizes the potentials used in this study and specifies the scenarios in which they have been applied.

#### A. Fitting Accuracy

We investigate the accuracy and the generalization of several fitted ACE models. We compare the performance of ACE models for multilayer twisted graphene systems, evaluating two scenarios: one where the model was trained on twisted bilayer configurations and another where it was trained on monolayer configurations. After developing these two models, we tested their force-fitting accuracy on monolayer, twisted bilayer, and twisted trilayer configurations separately. The results are summarized in Figure 4 and in Table II. The Kolmogorov-Crespi potential has fairly poor accuracy across all tests. The generic pacemaker C potential performs surprisingly well given it is trained primarily on bulk data, only being outperformed in accuracy by the ACE (\*) potential trained on mono-, bi- and trilayer structures. We will observe similar behaviour in many of the remaining tests.

Figure 4 provides a more detailed description of the force accuracy of the ACE potentials. In each column, the three subplots represent the predicted forces versus the DFT reference forces for monolayer, twisted bilayer, and twisted trilayer configurations, respectively. The results demonstrate that training only on mono-layer configurations (ACE (mo)) does not yield any acceptable generalization to bi- and tri-layers. This is unsurprising since the cutoff radius for the ACE potentials is larger than the interlayer distance. Training on only bilayer configurations results in moderately accurate generalization to both monolayer and twisted trilayer configurations. Note in particular that the generic `pacemaker` model [28] has far better accuracy on all multi-layers except bilayers.

The final potential trained on the filtered dataset, ACE (\*), provides significantly better accuracy across all multi-layers, validating both the accuracy and the generalization ability of the potential trained using the filtering strategy. Moreover, the results demonstrate that an ACE (\*) model trained on single, bi- and tri-layer configurations provides excellent accuracy also on quadrilayer and pentalayer configurations. This is likely due to a very short interaction distance in multi-layer graphene and it is unclear whether such a result would generalize to more complex materials.

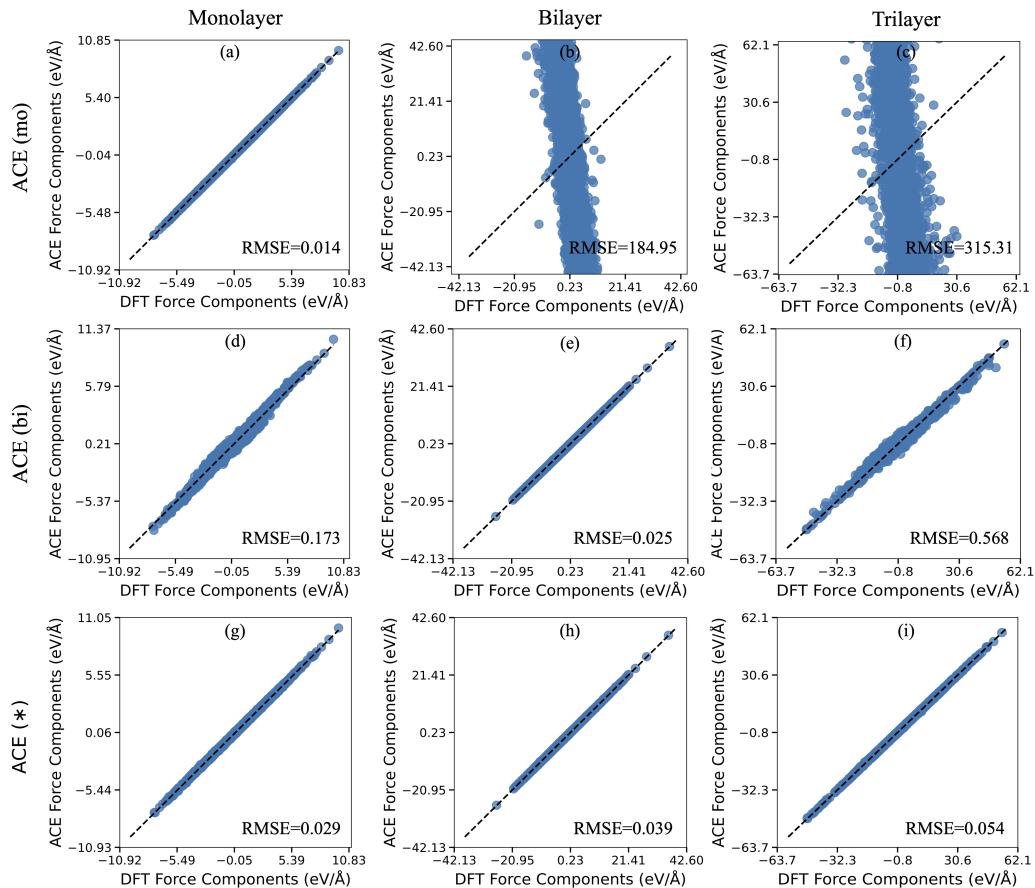


FIG. 4: Test accuracy for three ACE potentials: (a-c) for ACE (mo) trained only on mono-layer data, (d-f) for ACE (bi) trained on only bi-layer data and (g-i) for ACE (\*) trained on the full dataset described in § IIC; cf. Table I for further specifications of the three models.

TABLE II: Test accuracy in terms of RMSE (relative to DFT) for the three ACE potentials trained in this work, the pacemaker, and the KC potentials. All values are reported in  $\text{eV}/\text{\AA}$ . Entries with an RMSE below  $0.1 \text{ eV}/\text{\AA}$  are highlighted.

	Monolayer	Bilayer	Trilayer	quadrilayer	Pentalayer
KC	0.641	1.207	4.368	4.782	4.869
pacemaker	0.106	0.126	0.441	0.454	0.468
ACE (mo)	<b>0.014</b>	184.952	315.314	316.468	306.203
ACE (bi)	0.173	<b>0.025</b>	0.568	1.149	1.502
ACE (*)	<b>0.029</b>	<b>0.039</b>	<b>0.054</b>	<b>0.089</b>	<b>0.093</b>

## B. Geometry Optimization

We test the ability of the fitted ACE potentials to accurately predict equilibrium crystalline and defective structures. We perform geometry optimization experiments for various configurations of twisted multilayer graphene, including defect formation, defect migration, and stress-strain curves.

TABLE III: Validation of minimization for homogeneous and defected configurations in twisted bilayer systems with a twist angle of  $4.41^\circ$ . Here, a check mark ( $\checkmark$ ) indicates successful geometric relaxation, with the number in parentheses denoting the number of iterations required for convergence. A cross ( $\times$ ) indicates that the relaxation failed to converge. A large number of iterations or convergence failure indicate a non-smooth or even unphysical potential energy surface.

	Homogeneous	Vacancy	Stone-Wales	Interlayer interstitial	Intralayer interstitial
KC	$\checkmark$ (55)	$\checkmark$ (65)	$\checkmark$ (719)	$\checkmark$ (260)	$\checkmark$ (448)
pacemaker	$\checkmark$ (47)	$\checkmark$ (505)	$\checkmark$ (736)	$\checkmark$ (353)	$\checkmark$ (550)
ACE (gt)	$\checkmark$ (71)	$\checkmark$ (132)	$\times$	$\times$	$\times$
ACE (lt)	$\checkmark$ (48)	$\checkmark$ (257)	$\checkmark$ (394)	$\checkmark$ (257)	$\checkmark$ (360)
ACE (gl)	$\checkmark$ (47)	$\checkmark$ (224)	$\checkmark$ (309)	$\checkmark$ (253)	$\checkmark$ (298)
ACE (*)	$\checkmark$ (48)	$\checkmark$ (235)	$\checkmark$ (290)	$\checkmark$ (242)	$\checkmark$ (340)

### 1. Stability of structure equilibration

To facilitate comparison and to test the performance of the filtering strategy introduced in Section II C, we trained several ACE models using different dataset combinations. The model trained using the filtering strategy described in Section II C is denoted by ACE (\*). We compare against ACE models trained on a variety of randomly selected globally and locally twisted datasets; see Table I for the details.

The systems for which we conduct geometry optimization include twisted bilayer graphene with a twist angle of  $4.41^\circ$ , both pure and with point defects, including vacancies, Stone-Wales (SW) defects [67], intralayer interstitials and interlayer interstitials. The geometry minimization solver used is L-BFGS [68], with a force tolerance set to  $10^{-3}$  eV/Å. Our results show that only models trained on both globally and locally twisted configurations perform reliably across all tests.

Table III summarizes geometry optimization results for all models and all configurations. A check mark indicates that the minimization procedure successfully converged to a local minimum, while a cross mark signifies that the procedure either failed or did not converge within the 1000 iterations. An unsuccessful optimisation typically entails energies decreasing into the negative thousands of eV range and forces reaching  $O(10^5)$  eV/Å range. The models trained using the filtering strategy and those trained on locally twisted configurations, as introduced in Section II C, performed well, consistently achieving equilibrium structures for all defective cases. Models trained solely on globally twisted configurations failed to converge for the interlayer and intralayer interstitial cases, likely due to the stronger interactions in those cases. The KC and pacemaker potentials also converged successfully for all cases.

Table IV presents analogous results of geometry relaxation for five commensurate twisted bilayer graphene configurations with twist angles ranging from  $4.41^\circ$  to  $33.65^\circ$ . Models trained using the filtering strategy and those trained on locally twisted configurations (introduced in Section II C) performed well. In contrast, models trained exclusively on globally twisted configurations failed to converge for the largest twist angle of  $33.65^\circ$ , likely due to extrapolation challenges.

The number of optimization steps shown in brackets are an indicator of the smoothness of the potential energy surface, facilitating comparisons across different interatomic potentials (e.g., ACE, KC, pacemaker). By this measure, all ACE models using locally twisted training structures exhibits superior convergence behavior, suggesting a qualitatively smoother energy landscape.

### 2. Defect formation energies

The previous section demonstrates the stability of geometry optimization. Next, we test quantitative accuracy of the predicted minimizer by comparing predicted defect formation energies against their corresponding DFT values. These tests assess out-of-distribution performance, since the training set does not contain defective structures. The defect-free system is a  $4.41^\circ$  degree twisted bilayer structure containing 676 atoms. Interatomic forces are relaxed in all the systems using the trained interatomic potentials. The reference DFT energetics are computed on the relaxed structures using the trained potentials. Further relaxation of DFT interatomic forces is not conducted. Given that the model ACE (gt) trained only on globally twisted configurations does not perform well, we limit these tests to the ACE (lt), ACE (gl) and ACE (\*) models. The results are summarized in Table V. We observe that the ACE (\*) model (generated using the active learning strategy) provides significantly higher accuracy on all tests, with the exception

TABLE IV: Validation of minimization for commensurate twisted bilayer configurations with various twist angles.

Twisted angles	4.41°	16.43°	24.21°	29.64°	33.65°
Number of atoms	676	196	3844	7396	1444
KC	✓ (49)	✓ (26)	✓ (27)	✓ (28)	✓ (26)
pacemaker	✓ (43)	✓ (26)	✓ (23)	✓ (26)	✓ (24)
ACE (gt)	✓ (38)	✓ (32)	✓ (27)	×	×
ACE (lt)	✓ (37)	✓ (28)	✓ (31)	✓ (33)	×
ACE (gl)	✓ (35)	✓ (31)	✓ (27)	✓ (34)	✓ (39)
ACE (*)	✓ (36)	✓ (30)	✓ (29)	✓ (32)	✓ (41)

TABLE V: Point defect formation energies in bilayer graphene with a twist angle of 4.41° for three ACE potentials. The relative error is given in the bracket. Entries within  $\pm 5\%$  of the reference values and the best-performing results across all methods are highlighted.

	Vacancy	Stone-Wales	Interlayer interstitial	Intralayer interstitial
DFT	8.419	4.948	9.017	7.883
KC	7.707 (-8.46%)	5.430 (9.74%)	12.463 (38.22%)	7.183 (-8.88%)
pacemaker	7.053 (-16.23%)	<b>4.960 (-0.24%)</b>	7.867 (-12.75%)	6.797 (-13.78%)
ACE (lt)	7.186 (-14.64%)	5.710 (15.41%)	7.221 (-19.91%)	6.408 (-18.70%)
ACE (gl)	7.825 (-7.06%)	5.540 (11.97%)	7.885 (-12.55%)	6.971 (-11.57%)
ACE (*)	<b>8.103 (-3.75%)</b>	<b>5.144 (3.96%)</b>	<b>8.256 (-8.44%)</b>	<b>8.031 (1.88%)</b>

of a single test where the pacemaker potential achieves slightly better accuracy. The models trained solely on locally twisted configurations and those trained on combined data all show relatively crude accuracy, comparable with the general purpose pacemaker potential.

### 3. Equilibration of twisted trilayer graphene

We perform geometry optimization of trilayer graphene with alternating twist angle of  $\pm 4.41^\circ$ . This test is restricted to the ACE (gt) and ACE (lt) potentials. Figure 5 visualizes the two computed equilibrium structures. The potential ACE (lt) trained on locally twisted configurations predicts a realistic equilibrium structure. By contrast, the potential ACE (gt) trained only on globally twisted configurations predicts an equilibrium with noticeable undulations and distortions in the layers, indicating significant interlayer interactions that are incorrectly predicted. The ACE (\*) model shows similar performance to the ACE (lt) model.

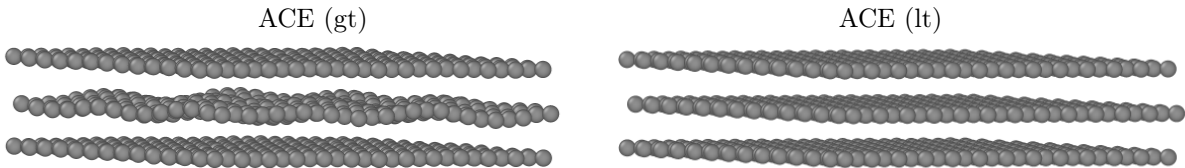


FIG. 5: Equilibrium structure of alternately twisted 4.41° trilayer graphene, minimized using the ACE (gt) potential trained on globally twisted configurations (**left**) and the ACE (lt) potential trained on locally twisted configurations (**right**). The unphysical out-of-plane displacement in the left-hand figure are approximately 1.1Å.

#### 4. Vacancy migration

As a more stringent out-of-distribution test we now consider the prediction of a vacancy migration pathway, calculated using the Nudged Elastic Band (NEB) method [69]. We consider a single vacancy in the upper layer of bilayer graphene with a twist angle of  $4.41^\circ$ . This test is restricted to the ACE (\*) model trained using the filtering approach, and to the pacemaker and KC comparison potentials. This is an out-of-distribution test: the training sets for neither MLIPs employed in this test contain any defect structures, and in particular do not contain structures close to the target migration pathway.

The results are reported in Figure 6. While both the pacemaker and KC models fail to predict qualitatively reasonable migration profiles, the ACE (\*) potential predicts an energy path and transition energy barrier that are qualitatively correct and only have a moderately small error when compared against the DFT predictions. To assess the impact of fine-tuning, we include the DFT reference configurations along the NEB path in the training set and retrain the model. The fine-tuned model, ACE (ft), shows improved accuracy and in particular reproduces the DFT energy barrier.

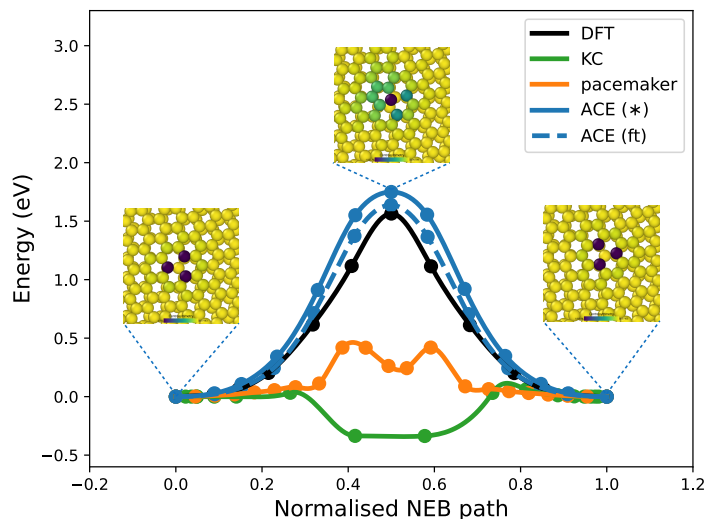


FIG. 6: The NEB path for a vacancy migration in twisted bilayer graphene (cf. Sec. III B 4), migration energy barrier and the defect core structures of initial, saddle and final states along the NEB path. Only the ACE (\*) and its fine-tuned potential, ACE (ft), provide a qualitatively correct prediction.

#### 5. Stress-strain curves

Stress-strain curves offer essential insight into the mechanical behavior of materials, particularly their elastic properties and failure mechanisms. In multilayer graphene, this response is highly sensitive to stacking order, interlayer interactions, and structural defects. In this section, we evaluate the stress-strain behavior of several multilayer graphene systems under uniaxial tension to assess the mechanical trends and the predictive capability of the fitted ACE (\*) potential. Since our potentials were not trained on strained systems, this is a (mild) out-of-distribution test, hence we cannot expect high accuracy.

Starting from fully relaxed atomic structures, with both atomic positions and cell parameters optimized, we apply uniaxial strain along the armchair direction by incrementally increasing the deformation up to 20%. At each strain level, the structure is re-relaxed using the L-BFGS algorithm [70] with a force convergence threshold of  $0.001\text{eV}/\text{\AA}$ , while keeping the cell fixed along the transverse directions. The virial stress tensor is then computed to extract the longitudinal stress component.

We examine several representative systems, including monolayer graphene, bilayer graphene with a twist angle of  $4.41^\circ$ , and trilayer graphene with alternating twist angles of  $\pm 4.41^\circ$ . Additionally, we consider bilayer configurations with point defects such as vacancies, Stone–Wales defects, and interlayer interstitials. The resulting stress-strain curves are shown in Figure 7. In the linear elastic regime, the slope of each curve yields the Young’s modulus,  $E = \sigma/\epsilon$ , characterizing the stiffness of the material. Among the systems studied, the trilayer structure exhibits the highest Young’s modulus, indicating increased stiffness with additional layers. The trends are consistent with

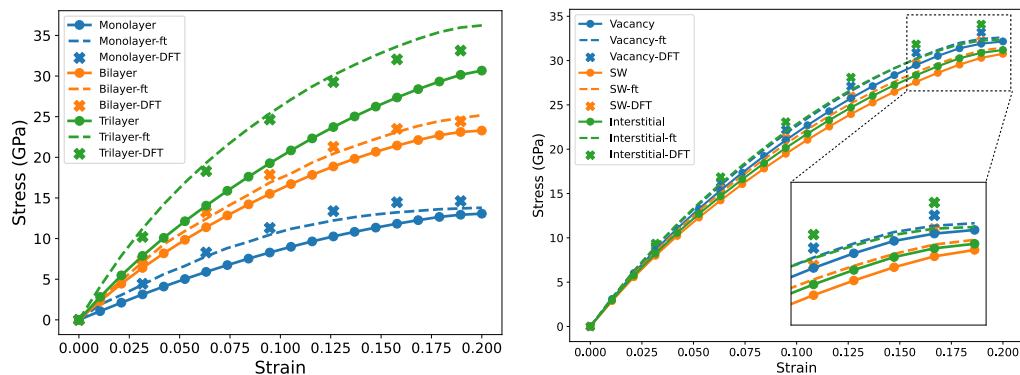


FIG. 7: Stress-strain curves computed using the ACE (\*) potential and the fine-tuned ACE potentials. **Left:** Monolayer, bilayer (with a twist angle of  $4.41^\circ$ ), and trilayer (with alternating twist angles of  $\pm 4.41^\circ$ ) graphene under uniaxial tension along the armchair direction. **Right:** Trilayer graphene systems containing different types of point defects, including a single vacancy, a Stone-Wales (SW) defect, and an interlayer interstitial.

DFT reference calculations. We also examine the effect of fine-tuning by incorporating the DFT reference strained configurations into the training set and retraining the model. The resulting fine-tuned model exhibits clear improved agreement with the DFT reference across both test cases.

### C. Molecular Dynamics

After systematically examining the accuracy and stability of the fitted ACE models in geometry optimization tasks, we now conduct similar tests of the models' performance in molecular dynamics (MD) simulations. All molecular dynamics simulations performed in this section were conducted using a Langevin thermostat, targeting the desired temperature with a friction coefficient of  $0.01 \text{ fs}^{-1}$  and 1fs time-step. As in the previous section, we use twisted bilayer configurations with a twist angle of  $4.41^\circ$  throughout this section unless otherwise specified.

#### 1. MD Stability

We perform molecular dynamics simulations of  $4.41^\circ$  twisted bilayer graphene at 1000K, using the ACE (gt) and ACE (lt) potentials. The results are shown in Figure 8. The MD simulation using ACE (gt) (trained only on globally twisted configurations) becomes unstable after around 2500 time steps. After this point, the temperature rises sharply, accompanied by significant changes in the potential energy and pressure. This confirms our previous observations that the potential energy surface generated by the ACE (gt) model, trained only on globally twisted configurations, contains "unstable regions" that lead to non-physical behavior in the simulations. By contrast, the MD simulation using ACE (lt) (trained on locally twisted configurations) remains stable for the entire trajectory of 20,000 steps, further supporting the value of using locally twisted configurations during model training.

Next, we demonstrate the stability of MD for bilayer graphene in a large domain and much longer simulation time, only for the ACE (\*) potential. Specifically, we analyze thermodynamic stability for a single unit cell of  $29.64^\circ$  twisted bilayer graphene with an interlayer interstitial defect. The total number of atoms in the system is 7397. We perform MD simulation of this system at 1000K for  $10^5$  time steps. The results are shown in Figure 9. The fast equilibration followed by stable fluctuations of energy, temperature and pressure over this trajectory indicates long-time stability of the MD system.

#### 2. Dynamical properties

Next we present results on dynamic properties, including diffusion coefficients [71] and the velocity auto-correlation function (VACF). For these tests we can no longer compare to reference DFT predictions, hence these tests only confirm the robustness and qualitative correctness of our model for these simulation tasks.

The diffusion coefficient in twisted bilayer graphene is important for understanding its ability to intercalate (e.g., by lithium), and thus access its potential as an energy material candidate [72]. It can be computed from atomic

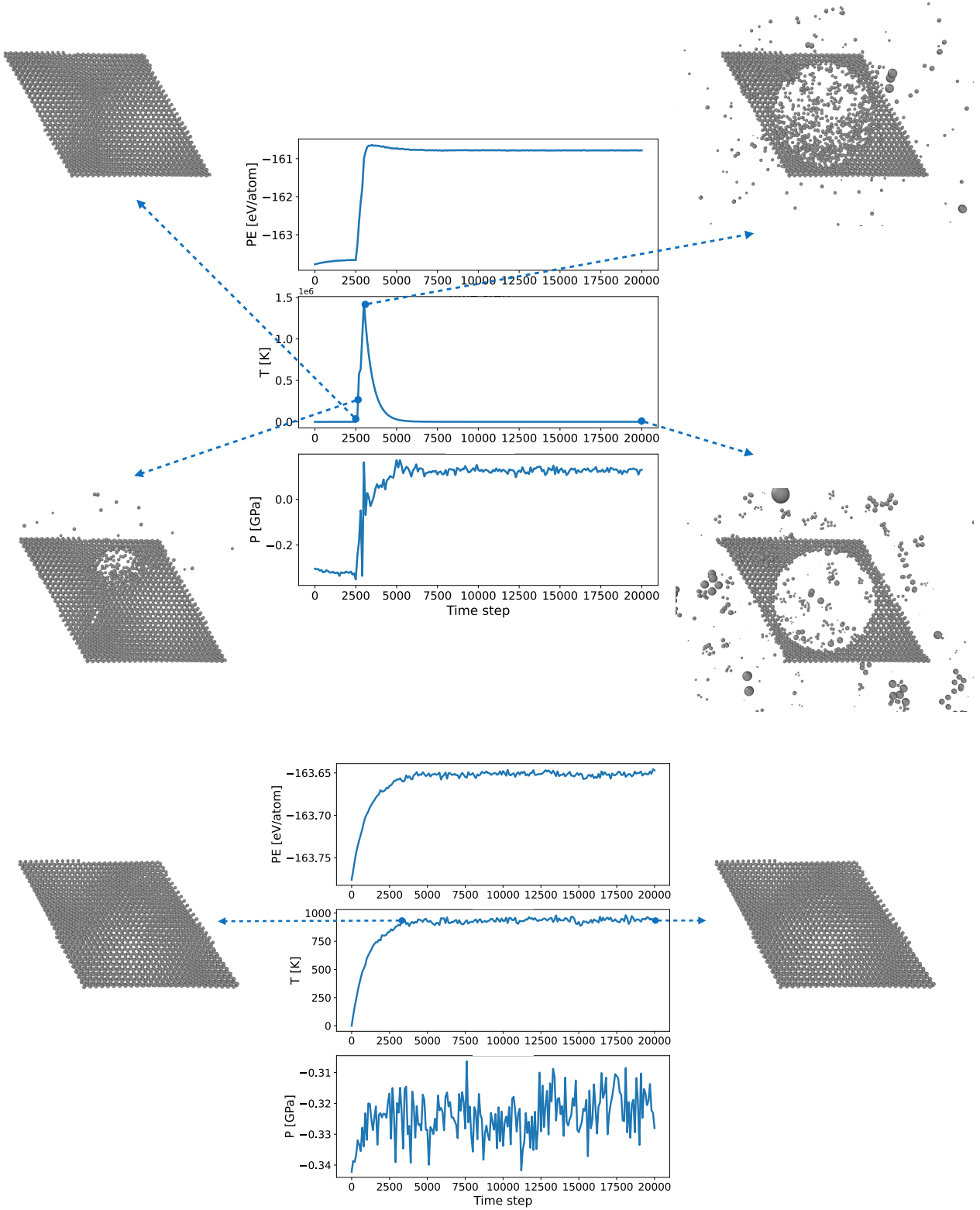


FIG. 8: Trajectories and thermodynamic properties from molecular dynamics simulations of  $4.41^\circ$  twisted bilayer graphene at 1000K using the ACE (gt) potential (Top) and the ACE (lt) potential (Bottom). The ACE (gt) potential trained only on globally twisted results in unstable behaviour, while dynamics under potential ACE (lt) remains stable for the entire trajectory.

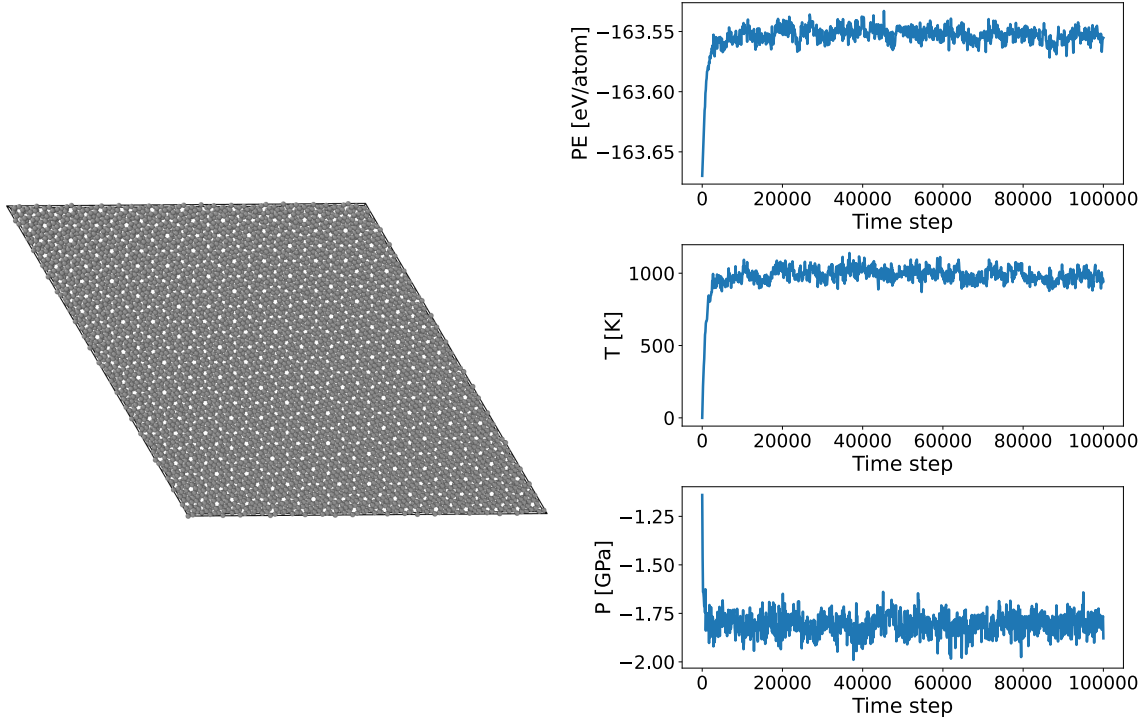


FIG. 9: **Left:** Atomic configuration of a commensurate unit cell of bilayer graphene twisted by  $29.64^\circ$ , featuring an interlayer interstitial defect, containing a total of 7397 atoms. **Right:** Evolution of thermodynamic properties at 1000K over  $10^5$  molecular dynamics steps. The potential exhibits stable molecular dynamics for the entire trajectory.

trajectories obtained via molecular dynamics (MD) simulations using the mean squared displacement (MSD) as a function of time, [73]

$$D = \lim_{t \rightarrow \infty} \frac{\langle |\mathbf{r}(t) - \mathbf{r}(0)|^2 \rangle}{6t}, \quad (12)$$

where  $\mathbf{r}(t)$  is the particle position at time  $t$  and angular brackets  $\langle \cdot \rangle$  denotes the canonical average, approximated in practice as an average over all particles in the system and multiple samples of time origins along the MD trajectory.

We compute the diffusion coefficients using the above formulation and present the results for various temperatures in Figure 10. The results align with the expectation that the diffusion coefficient increases with temperature. While [74] provides relevant results that do not account for temperature dependence, to the best of the authors' knowledge, no reference data or experimental results are currently available for direct comparison.

The velocity auto-correlation function (VACF) is another important dynamical property, providing insights into the temporal correlations of particle velocities in twisted bilayer graphene. The VACF  $C_v(t)$  can be computed from the velocities obtained from molecular dynamics simulations and is important for understanding thermal transport and the dynamic stability of the material [75]. The VACF  $C_v(t)$  is defined as:

$$C_v(t) = \langle \mathbf{v}(0) \cdot \mathbf{v}(t) \rangle, \quad (13)$$

where  $\mathbf{v}(t)$  is the velocity vector of a particle at time  $t$ , and  $\mathbf{v}(0)$  is the initial velocity vector of the particle. The angle brackets denote an ensemble average over all particles and time origins. In practice, the VACF is computed as:

$$C_v(t) = \frac{1}{N} \sum_{i=1}^N \frac{1}{T-t} \int_0^{T-t} \mathbf{v}_i(\tau) \cdot \mathbf{v}_i(\tau+t) d\tau, \quad (14)$$

where  $N$  is the number of particles, and  $T$  is the total simulation time.

In Figure 10, we present the velocity auto-correlation function (VACF) results for twisted bilayer graphene across various temperatures (100K, 300K, 500K, and 700K), plotted on a semi-logarithmic scale. This semi-log plot clearly

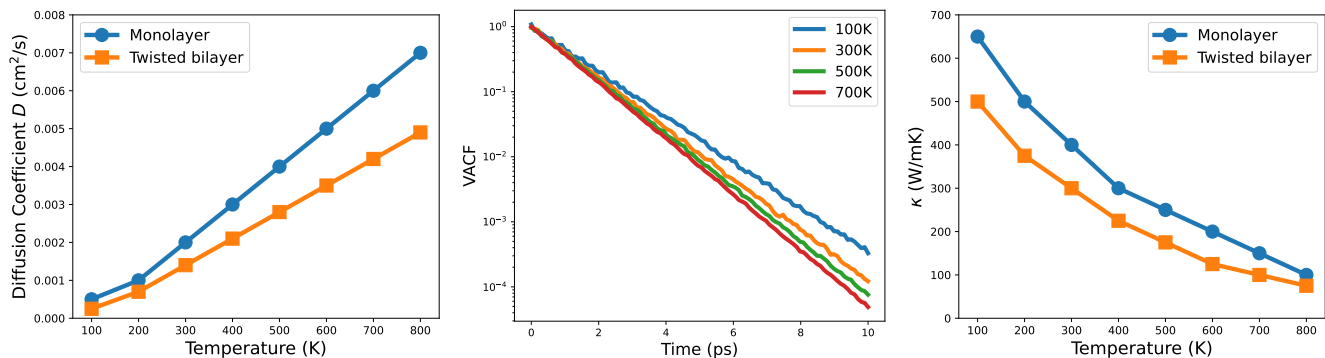


FIG. 10: **Left:** Diffusion coefficients of monolayer and twisted bilayer graphene for various temperatures. **Center:** The velocity auto-correlation function (VACF) of twisted bilayer graphene for various temperatures. **Right:** Thermal conductivity at various temperatures with the fitted ACE (\*) potential for monolayer and twisted bilayer graphene.

shows the exponential decay of the VACF over time, with the decay rate increasing as the temperature rises, indicating a faster loss of velocity correlation at higher temperatures. This trend reflects the enhanced atomic vibrations and thermal motion at elevated temperatures, which lead to quicker decorrelation in particle velocities.

Although finding direct references for comparison is challenging due to the long-time dynamics required, the shape and decay behavior of the VACF here are qualitatively correct. Such details are difficult to capture with conventional DFT, underscoring the utility and necessity of MLIPs in studying systems like twisted bilayer graphene.

Twisted bilayer graphene shows variations in thermal conductivity due to induced changes in electronic and phonon transport mechanisms [48, 76]. Compared to single-layer graphene, various twist angles can lead to diverse thermal behavior, highlighting the potential for tailoring graphene’s thermal properties through precise structural engineering [77]. Thermal conductivity in MD simulations reflects how heat is transferred at the atomic level. The Green-Kubo method [78], based on the fluctuation-dissipation theorem, is the most widely used approach for calculating thermal conductivity from equilibrium MD simulations. It is given by

$$\kappa = \frac{V}{k_B T^2} \int_0^\infty \langle J(0), J(t) \rangle dt, \quad (15)$$

where  $V$  is the system volume,  $k_B$  is the Boltzmann constant,  $T$  is the temperature,  $J(t)$  is the heat flux at time  $t$ , and  $\langle J(0), J(t) \rangle$  is the autocorrelation function of the heat flux. In practice, the integral is computed numerically, with the heat flux derived from the time evolution of atomic velocities and positions.

In twisted bilayer graphene, these parameters can be significantly altered by the twist angle. Experimental data indicate that the thermal conductivity of TBG is significantly lower than that of monolayer graphene and bilayer graphene. This phenomenon can be attributed to changes in the Brillouin zone and the emergence of additional phonon branches due to the twisted structure, which enhance phonon Umklapp and normal scattering [79, 80].

We provide a validation of thermal conductivity computed from the molecular dynamics trajectories in Figure 10. The results indicate that as the temperature increases, the thermal conductivity significantly decreases due to enhanced phonon-phonon scattering at high temperatures. The findings show good qualitative agreement with the literature [79].

#### D. Phonon Spectra

To conclude we assess the ability of the ACE (\*) model for predicting graphene phonon modes. The general phonon equation of motion is given by [81]

$$D_{\mu\nu\alpha\beta}(\mathbf{q})\delta u_{\nu\beta}(\mathbf{q}) = \omega^2 \delta u_{\mu\alpha}(\mathbf{q}), \quad (16)$$

where the subscripts  $\mu\nu$  denote the Cartesian coordinates,  $\alpha\beta$  refer to atomic indices,  $\mathbf{q}$  is the phonon momentum,  $\omega$  represents the phonon frequency, and  $\delta u$  is the phonon displacement field. The dynamical matrix element  $D_{\mu\nu\alpha\beta}(\mathbf{q})$  is defined as

$$D_{\mu\nu\alpha\beta}(\mathbf{q}) = \sum_j \tilde{D}_{\mu\nu\alpha\beta}(\mathbf{R}_j) e^{-i\mathbf{q}\cdot\mathbf{R}_j}, \quad \tilde{D}_{\mu\nu\alpha\beta}(\mathbf{R}_j) = \frac{1}{M} \frac{\partial^2 E^{\text{tot}}(\mathbf{A})}{\partial \mathbf{r}_{j\mu\alpha} \partial \mathbf{r}_{0\nu\beta}}. \quad (17)$$

Here,  $ij$  represent supercell indices for a  $5 \times 5$  grid of supercells with the central supercell indexed by  $i = 0$ ,  $\mathbf{R}_j$  are the supercell lattice vectors,  $\mathbf{r}_{i\mu\alpha}$  the atomic positions,  $\mathbf{A}$  the atomic structure, and  $M$  is the mass of the Carbon atom. The dynamical matrix elements are proportional to the derivatives of the forces. Phonon mode calculations via Density Functional Theory (DFT) typically involve either differentiating the forces by displacing atoms or employing Density Functional Perturbation Theory (DFPT). Both methods are computationally demanding. Both classical and machine learning interatomic potential models can be differentiated analytically to second order at relatively low computational cost.

We evaluate the performance of the fitted ACE (\*) potential on phonons in Fig. 11, showing also analogous results for the KC and pacemaker potentials for comparison. Results are shown for monolayer graphene, Bernal/AB-stacked bilayer graphene, and for twisted bilayer graphene at  $7.34^\circ$  commensurate angle.

For monolayer and for Bernal/AB-stacked bilayer graphene (rigid shift), ACE (\*) and DFT have an excellent agreement, with the exception of a moderate error in the layer breathing mode near  $\Gamma$ -point. For these two tests, the KC potential provides good qualitative but not quantitative agreement with DFT. For the optical phonons, both KC and pacemaker potential substantially deviate from the DFT results.

In the  $7.34^\circ$  twisted system, the overall shape of the low-energy phonons, such as folded acoustic phonons, is consistent with DFT predictions (see [81]). However, discrepancies appear along the M–K path, and most notably, moiré optical phonons near 10 meV are absent. The absence of the optical moiré potential is partially due to the overestimate of the layer breathing mode frequency at the  $\Gamma$ -point in AB bilayer graphene (Fig. 11(b)). With a twist angle, the moiré Brillouin zone becomes much smaller than the monolayer Brillouin zone, which amplifies the discrepancy in the relative frequencies between the folded acoustic modes and the optical modes.

In summary, the custom fitted ACE (\*) potential significantly outperforms both KC and pacemaker potentials in these tests, but still has limitations in high-energy modes and moiré optical phonons in twisted systems. Future work will investigate solutions to these limitations.

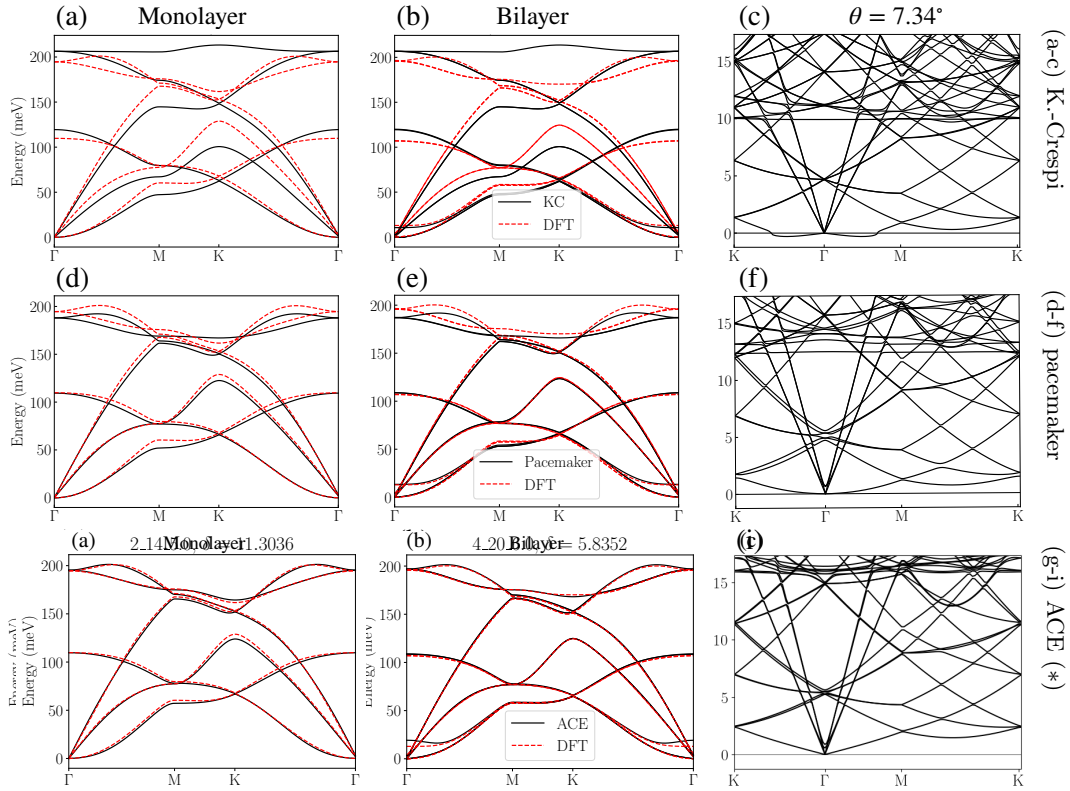


FIG. 11: Phonon band structures obtained from the ACE (\*) potential (a,b,c), Kolmogorov-Crespi potential (d, e, f) and the general purpose pacemaker C potential (g, h, i). Black solid lines represent the interatomic potentials generated phonon spectra while red dashed lines represent the DFT-generated results. Column (a, d, g) shows the results for monolayer graphene; column (b, e, h) for Bernal/AB-stacked bilayer graphene; column (c, f, i) for twisted bilayer graphene at  $7.34^\circ$  commensurate angle.

## IV. CONCLUSION

In this study, we have comprehensively explored the use of machine-learning interatomic potentials (MLIPs) to simulate the complex behavior of twisted multilayer graphene, a system characterized by its unique moiré patterns. By leveraging the Atomic Cluster Expansion (ACE) architecture, we developed an interatomic potential model that achieves near-DFT (in-distribution) accuracy while significantly reducing computational costs. Our approach introduces a new method to generate training and testing datasets using locally twisted structures capable of exhaustively sampling the large configuration space of twisted multilayered materials. The model's performance across a wide range of simulation tasks, including geometry optimizations, molecular dynamics simulations, and phonon calculations, demonstrates the effectiveness of the fitted model both in- and out-of-distribution. Our results demonstrate that the transferrability from non-specialized training datasets to predictions of general twist angles is not guaranteed, but that the locally twisted structures we propose are sufficient to guarantee stable and accurate predictions in a wide range of simulation tasks.

The model is therefore well suited as a starting point for an efficient and robust active-learning approach, adding unseen structures as required for new simulation tasks. It thus provides a theoretical framework for systematically and quantitatively exploring the properties of low-dimensional materials and bridging the gap between microscopic properties and experimental observations such as twist angle disorder [82] and strain [83], which are frequently encountered but often overlooked in theoretical models.

## V. ACKNOWLEDGEMENT

ML acknowledges support from NSF DMS 2422469. ML's research was also supported by a visit to the Kavli Institute for Theoretical Physics (NSF PHY-2309135) and by a visit to CCQ at the Simons Flatiron Institute for support while (a portion of) this research was carried out. DC acknowledges support by DoD NDSEG. VG and SD acknowledge the support from NSF DMS 2422470. CO acknowledges the support of the Natural Sciences and Engineering Research Council of Canada (NSERC) and support through computational resources and services provided by Advanced Research Computing at the University of British Columbia. ZZ is supported by a Stanford Science Fellowship. DM acknowledges support from NSF DMS 2422471. We finally acknowledge support for a collaboration visit at ICERM.

### Appendix A: Atomic Cluster Expansion (ACE)

We provide a brief review of the Atomic Cluster Expansion (ACE) model but refer to [16, 22, 84–87] for further details and discussion. Recalling the setup from Section II B, we consider an atomic configuration  $\mathbf{A} := \{\mathbf{r}_1, \dots, \mathbf{r}_N\} \in \mathbb{R}^{3N}$ , where  $N$  atoms are represented by their position vectors  $\mathbf{r}_j$ . The relative position vector between atom  $j$  and a reference atom  $i$  is  $\mathbf{r}_{ij} = \mathbf{r}_j - \mathbf{r}_i$ , and the *local* atomic environment around atom  $i$  with a cutoff radius  $r_{\text{cut}}$  is  $\mathbf{A}_i := \{\mathbf{r}_{ij}\}_{j \in \mathcal{N}(i)}$ , where  $\mathcal{N}(i)$  denotes the set of indices of all atoms within the cutoff radius  $r_{\text{cut}}$  from atom  $i$ .

The ACE site energy  $\varepsilon(\mathbf{A}_i; \mathbf{c})$  can be formulated as a body-order expansion for a given correlation order  $\nu_{\text{max}} \in \mathbb{N}$ ,

$$\varepsilon(\mathbf{A}_i; \mathbf{c}) = \sum_{\nu=0}^{\nu_{\text{max}}} \frac{1}{\nu!} \sum_{j_1, \dots, j_\nu \in \mathcal{N}(i)} V_\nu(\mathbf{r}_{ij_1}, \dots, \mathbf{r}_{ij_\nu}; \mathbf{c}), \quad (\text{A1})$$

where the  $(\nu + 1)$ -body potential  $V_\nu : \mathbb{R}^{3\nu} \rightarrow \mathbb{R}$  is approximable by using a tensor product basis [22],

$$\phi_{n\ell m}(\mathbf{r}_{ij_1}, \dots, \mathbf{r}_{ij_\nu}) := \prod_{\alpha=1}^{\nu} \phi_{n_\alpha \ell_\alpha m_\alpha}(\mathbf{r}_{ij_\alpha}),$$

and the one-body basis is given by  $\phi_{n\ell m}(\mathbf{r}) := P_n(y)Y_\ell^m(\hat{\mathbf{r}})$ , with  $\mathbf{r} \in \mathbb{R}^d$ ,  $r = |\mathbf{r}|$ , and  $\hat{\mathbf{r}} = \mathbf{r}/r$ . The functions  $Y_\ell^m$  denote the complex spherical harmonics for  $\ell = 0, 1, \dots$ , and  $m = -\ell, \dots, \ell$ , and  $P_n$  are radial basis functions for  $n = 0, 1, \dots$ . This parametrization is already invariant under permutations (or, relabeling) of the input local atomic environment  $\mathbf{A}_i$ . One then symmetrizes the tensor product basis with respect to the group  $O(3)$ , employing the representation of that group in the spherical harmonics basis. This results in a linear parametrization of the terms of

correlation order  $\nu$

$$\begin{aligned} \varepsilon(\mathbf{A}_i; \mathbf{c}) &= \sum_{\mathbf{n}\ell q} c_{\mathbf{n}\ell q} \mathbf{B}_{\mathbf{n}\ell q}(\mathbf{A}_i), \\ \text{where } \mathbf{B}_{\mathbf{n}\ell q}(\mathbf{A}_i) &= \sum_{\mathbf{m} \in \mathcal{M}_\ell} C_{\mathbf{m}}^{\mathbf{n}\ell q} \mathbf{A}_{\mathbf{n}\ell\mathbf{m}}(\mathbf{A}_i), \\ \text{and } \mathbf{A}_{\mathbf{n}\ell\mathbf{m}}(\mathbf{A}_i) &= \prod_{\alpha=1}^{\nu} \sum_{j \in \mathcal{N}(i)} \phi_{\mathbf{n}_\alpha \ell_\alpha \mathbf{m}_\alpha}(\mathbf{r}_{ij}). \end{aligned}$$

In the above, the  $q$ -index enumerates the number of all possible invariant couplings through the generalized Clebsch-Gordan coefficients  $C_{\mathbf{m}}^{\mathbf{n}\ell q}$ ,  $\mathcal{M}_\ell := \{\mathbf{m} \in \mathbb{Z}^\nu \mid -\ell_\alpha \leq \mathbf{m}_\alpha \leq \ell_\alpha\}$ .

This parametrization was originally devised in [16]. Its approximation properties and computational complexity are analyzed in detail in [22, 88, 89]. The implementation we employ in our work is described in [64]. The latter reference also described the details of the choice of radial basis  $P_n$ .

To complete the description of our parametrization, we select a finite subset of the basis,

$$\begin{aligned} \mathcal{B} := \left\{ \mathbf{B}_{\mathbf{n}\ell q} \mid (\mathbf{n}, \ell) \in \mathbb{N}^{2\nu} \text{ ordered, } \sum_{\alpha} \ell_{\alpha} \text{ even, } \sum_{\alpha} \mathbf{m}_{\alpha} = 0, \right. \\ \left. q = 1, \dots, n_{\mathbf{n}\ell}, \sum_{\alpha} \ell_{\alpha} + \mathbf{n}_{\alpha} \leq D_{\text{tot}}, \nu \leq \nu_{\text{max}} \right\}, \end{aligned}$$

where the two approximation parameters are the correlation order  $\nu_{\text{max}}$  and the total degree  $D_{\text{tot}}$ . To facilitate the use of permutation invariance, we define  $(\mathbf{n}, \ell) \in \mathbb{N}^{2\nu}$  as ordered if the vector associated with this tuple is lexicographically ordered [22, Definition 1]. Additionally, we impose the condition that  $\sum_{\alpha} \ell_{\alpha}$  must be even to ensure point reflection symmetry. The constraint  $\sum_{\alpha} \mathbf{m}_{\alpha} = 0$  arises from the requirement that rotationally invariant basis functions are constructed using specific linear combinations of spherical harmonic products, which couple to a total angular momentum of zero. This property is derived purely within the framework of linear algebra. For a more detailed discussion, we refer the reader to [22, Section 3.4]. With this selection of the basis we can write our ACE parametrization more conveniently as

$$\varepsilon(\mathbf{A}_i; \mathbf{c}) = \sum_{\mathbf{B} \in \mathcal{B}} c_{\mathbf{B}} \mathbf{B}(\mathbf{A}_i), \quad (\text{A2})$$

where  $\mathbf{c} = \{c_{\mathbf{B}}\}_{\mathbf{B} \in \mathcal{B}}$  are the model parameters. Due to the completeness of this representation, as the approximation parameters (correlation order  $\nu_{\text{max}}$ , cut-off radius  $r_{\text{cut}}$ , and total degree  $D_{\text{tot}}$ ) approach infinity, the model can *in principle* represent any arbitrary potential [22].

Due to the rapid developments in MLIPs architectures and software, performance benchmarks would quickly become outdated. We therefore chose to not perform such benchmarks as part of our study. However, we briefly mention that the implementation we used at the time of writing has an inference cost of approximately  $100\mu\text{s}$  per atom for mono-layer graphene and approximately  $200\mu\text{s}$  per atom for bilayer graphene in single-threaded execution on a AMD EPYC-Rome (2000 MHz) CPU. We expect that designing a multi-layer graphene MLIP with primarily performance optimizations in mind can achieve comparable accuracy with significantly improved performance characteristics.

## Appendix B: Bayesian Linear Regression

In this section, we discuss the Bayesian linear regression that originally comes from the minimization of the loss (cf. (7)). Since all observations we consider here are linear, the minimization of  $\mathcal{L}(\mathbf{c})$  can be written in the form of the ridge regression

$$\underset{\mathbf{c}}{\text{argmin}} \|\mathbf{W}(\mathbf{O} - \Psi\mathbf{c})\|^2 + \lambda \|\Gamma\mathbf{c}\|^2, \quad (\text{B1})$$

where  $\mathbf{O}$  is a vector containing the observation values  $E^{\text{ref}}$ ,  $F^{\text{ref}}$ , and  $V^{\text{ref}}$ ,  $\Psi$  is the design matrix containing the ACE basis values corresponding to those observations, and  $\mathbf{W}$  is a diagonal matrix containing the weights  $w_{E, \mathbf{R}}$  and  $w_{F, \mathbf{R}}$ .  $\Gamma$  specifies the form of the regularizer and  $\lambda$  is a scaling parameter determining the relative weight of the regularization. This formulation of the least squares problem is often also called regularized least squares, and the  $\lambda \|\Gamma\mathbf{c}\|^2$  term is often called generalized Tikhonov regularization. The default for  $\Gamma$  is zero or the identity, depending on the choice of solver. Our recommendation is to use the smoothness prior introduced in [64] instead for most solvers.

Uncertainty estimates of model predictions are highly sought after tools to judge the accuracy of a prediction during simulation with a fitted model, but can also be employed to great effect during the model development workflow, e.g., in an active learning context. Such uncertainty estimates can be derived in a principled way by recasting the minimization problem (7) in a Bayesian framework where inference is based on the Bayesian posterior distribution

$$\text{post}(\mathbf{c}) := p(\mathbf{c}|\Psi, \mathbf{O}) \propto p(\mathbf{O}|\Psi, \mathbf{c})p(\mathbf{c}). \quad (\text{B2})$$

Here,  $p(\mathbf{O}|\Psi, \mathbf{c})$  denotes the likelihood of the observed data, and  $p(\mathbf{c})$  the prior distribution on the model parameters. The Bayesian analogue of (7) is a Bayesian Linear Regression model with Gaussian observational noise and prior

$$\begin{aligned} p(\mathbf{O}|\Psi, \mathbf{c}) &\propto \exp\left(-\frac{1}{2}(\mathbf{O} - \Psi\mathbf{c})^T(\beta\mathbf{W}^2)(\mathbf{O} - \Psi\mathbf{c})\right), \\ p(\mathbf{c}) &\propto \exp\left(-\frac{1}{2}\mathbf{c}^T\mathbf{\Sigma}_0^{-1}\mathbf{c}\right), \end{aligned} \quad (\text{B3})$$

where the covariance  $\beta^{-1}\mathbf{W}^{-2}$  of the observation noise depends on the regression weight matrix  $\mathbf{W}$  defined in (B1) and a hyperparameter  $\beta > 0$ .  $\mathbf{\Sigma}_0$  is the covariance matrix of prior  $p(\mathbf{c})$ . This choice of prior and noise model yields a Gaussian posterior distribution,  $p(\mathbf{c}|\Psi, \mathbf{O}) = \mathcal{N}(\mathbf{c}; \bar{\mathbf{c}}, \mathbf{\Sigma})$ , with mean and covariance given, respectively, by  $\bar{\mathbf{c}} = \beta\mathbf{\Sigma}\Psi^T\mathbf{W}^2\mathbf{O}$  and  $\mathbf{\Sigma} = (\beta\Psi^T\mathbf{W}^2\Psi + \mathbf{\Sigma}_0^{-1})^{-1}$ . The above Bayesian model can be connected to the ridge regression formulation of (B1) by noticing that maximising the posterior density (B2) is equivalent to minimizing the regularized loss in (B1) when  $\mathbf{\Sigma}_0^{-1} = \zeta\mathbf{I}^2$  for some  $\zeta > 0$  and  $\lambda = \zeta/\beta$ .

The reliability of uncertainty estimates critically depends on the values of the model hyper-parameters, the noise and prior covariance matrices  $\beta^{-1}\mathbf{W}^{-2}$  and  $\mathbf{\Sigma}_0$ . In ACE, it is sometimes difficult to make informed guesses of explicit values of these hyper-parameters that lead to good fits. We therefore commonly employ empirical Bayes approaches that infer appropriate values of these parameters directly from the training data by virtue of maximizing the model evidence.

$$\begin{aligned} p(\mathbf{O}|\Psi, \mathbf{\Sigma}_0, \beta) &= \int p(\mathbf{O}|\Psi, \mathbf{c}, \beta)p(\mathbf{c}|\mathbf{\Sigma}_0)d\mathbf{c} \\ &= \sqrt{\frac{\beta(2\pi)^{-N_{\text{obs}}|\mathbf{\Sigma}|}}{|\mathbf{\Sigma}_0||\mathbf{W}^{-2}|}} \exp\left(-\frac{1}{2}(\mathbf{O} - \Psi\bar{\mathbf{c}})^T(\beta\mathbf{W}^2)(\mathbf{O} - \Psi\bar{\mathbf{c}}) - \frac{1}{2}\bar{\mathbf{c}}^T\mathbf{\Sigma}_0^{-1}\bar{\mathbf{c}}\right) \end{aligned} \quad (\text{B4})$$

as a function of  $\mathbf{\Sigma}_0, \beta$ . Intuitively, maximizing the model evidence results in a model where the regularizing effect of the covariance matrix  $\mathbf{\Sigma}_0$  and the degree of penalization of model misfit—modeled by the noise covariance matrix  $\beta^{-1}\mathbf{W}^{-2}$ —are balanced against the degree to which the regression coefficients are determined by the data.

The Bayesian ridge solver provides a posterior parameter distribution  $p(\mathbf{c})$ . It remains important to estimate the uncertainty of predictions. Evaluating such uncertainties from the exact posterior distribution is computationally expensive; so one can draw  $K$  samples  $\{\mathbf{c}_k\}_{k=1}^K$  from  $\text{post}(\mathbf{c})$  resulting in a committee of ACE models which can be used to obtain computationally efficient uncertainty estimates for predictions. For example, the standard deviation  $\sigma$  of a total energy prediction can be approximated by a committee via

$$\sigma^E = \sqrt{\frac{1}{\beta w_{E,R}^2} + \frac{1}{K} \sum_{k=1}^K (E^k - \bar{E})^2}, \quad (\text{B5})$$

where  $\bar{E} := \sum_{i=1}^N \sum_{\mathbf{B} \in \mathcal{B}} \bar{\mathbf{c}} \cdot \mathbf{B}(\mathbf{A}_i)$  with  $\bar{\mathbf{c}}$  being the posterior mean of the distribution and  $E^k$  denoting the total ACE energy evaluated using  $\mathbf{c}^k$ . Similarly, the corresponding relative force uncertainty, as defined in [25], is given by:

$$\sigma_i^F := \frac{1}{K} \sum_{k=1}^K \frac{\|F_i^k - \bar{F}_i\|}{\|\bar{F}_i\| + \varepsilon},$$

where  $\bar{F}_i$  is the mean force prediction, and  $\varepsilon$  is a regularization constant to prevent divergence, typically set to around 0.2 eV/Å.

### Appendix C: Training Details

The DFT computations of the graphene layers in this work were performed using the DFT-FE software [90–93], a massively parallel open-source software for real-space Kohn-Sham DFT calculations using a systematically convergent

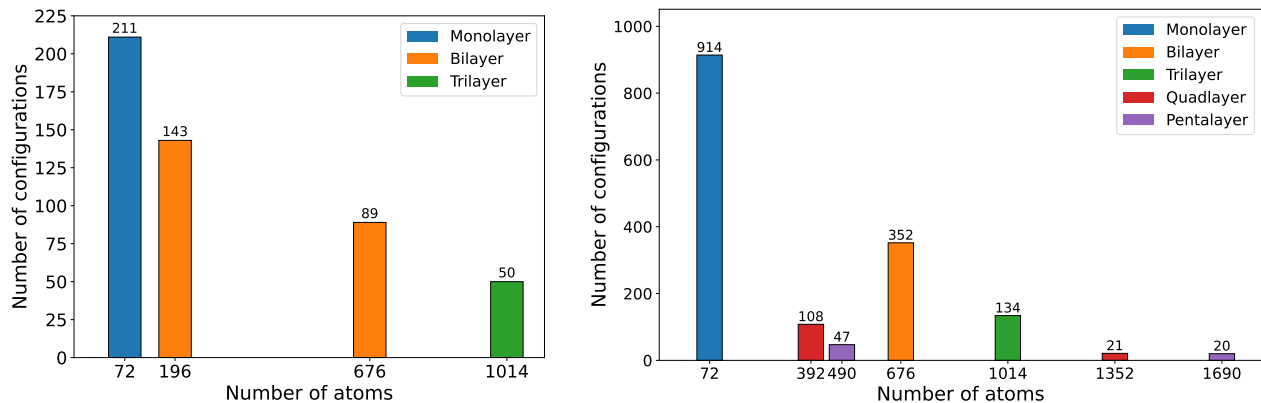


FIG. 12: Distribution of configuration counts with respect to the number of atoms in the training and test sets. Left: training set used for ACE model fitting; Right: test set corresponding to the results reported in Table II.

adaptive spectral finite-element discretization. DFT-FE employs the Chebyshev filtering acceleration technique [93, 94] for solving the Kohn-Sham eigenvalue problem, which in conjunction with mixed precision algorithms [95] provides a computational complexity for DFT-FE that scales quadratically with the number of electrons up to system sizes of 30,000 electrons [91]. The forces and stress tensor are computed using the configurational forces approach [92]. Further, the GPU acceleration of the code enables fast and accurate large-scale DFT calculations using DFT-FE [90, 95, 96]. The DFT training data was generated on system sizes up to 1014 atoms, the largest systems corresponding to trilayer graphene. The largest system sizes for which the DFT data was obtained for testing included up to 1352 atoms for quadrilayer graphene and 1690 atoms for pentalayer graphene. We employ the PBE exchange-correlation functional and the optimized norm-conserving Vanderbilt pseudopotentials (ONCV) [97] from the SPMS library [98]. All numerical parameters in DFT-FE were chosen such that the ground-state energies and interatomic forces are converged to an accuracy of under 3 meV/atom and 8 meV/Å, respectively. Additionally, we used a Fermi-Dirac smearing with a temperature of 500 K for all simulations. We note that the DFT-D3 [65] long-range dispersion corrections are added separately to the ACE model trained only with PBE exchange-correlation functional-based data. Figure 12 shows the distribution of configuration counts as a function of the number of atoms in the training and test sets.

#### Appendix D: Dataset Disregistry Generation

The choice of the disregistry in the local twisting method allows us to sample any point in the moiré unit cell. The local twisting method produces a structure with a central disk of radius  $r_1$  that matches the configuration of an  $r_1$  radius disk in the moiré cell. The location of this corresponding disk in the moiré cell is determined by the disregistry used in the local twisting method. So to ensure the entire moiré cell is present in the locally twisted configurations we just have to pick disregistries such that disks of radius  $r_1$  centered on each disregistry cover the moiré cell, i.e., our set of disregistries must be an  $r_1$ -covering of the moiré cell. Since the moiré cell size grows as the angle decreases, more disregistries are needed to cover smaller local twist angles than larger ones. The procedure we used was as follows: pick a starting point  $p_1$  on a diagonal of the moiré cell that is  $r_1$  distance away from a corner. Find the minimum spacing needed so that an evenly spaced grid including  $p_1$  aligned with the boundaries of the unit cell covers the cell. Some example disregistry grids generated with this method for various angles are shown in Figure 13.

The data and code will be made available upon publication via a GitHub repository.

- 
- [1] K. S. Novoselov, V. I. Fal'ko, L. Colombo, P. R. Gellert, M. G. Schwab, and K. Kim. A roadmap for graphene. *Nature*, 490(7419):192–200, 2012.
  - [2] F. Bonaccorso, Z. Sun, T. Hasan, and A. C. Ferrari. Graphene photonics and optoelectronics. *Nature Photonics*, 4(9):611–622, 2010.
  - [3] Y. Cao, V. Fatemi, S. Fang, K. Watanabe, T. Taniguchi, E. Kaxiras, and P. Jarillo-Herrero. Unconventional superconductivity in magic-angle graphene superlattices. *Nature*, 556(7699):43–50, 2018.

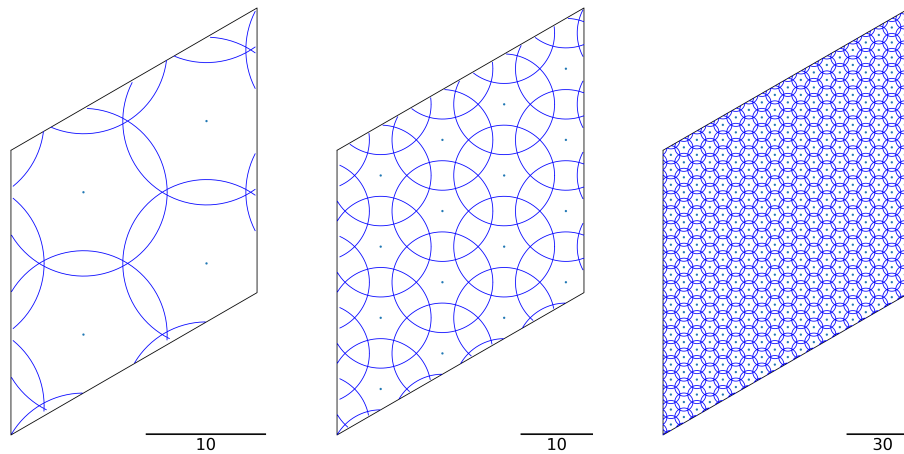


FIG. 13: Moiré unit cell with covering  $r_1$  radius circles centered on disregistry points chosen for various twist angles:  $6.0^\circ$  (left),  $3.6^\circ$  (middle),  $1.2^\circ$  (right).

- [4] R. Bistritzer and A. H. MacDonald. Moiré bands in twisted double-layer graphene. *Proceedings of the National Academy of Sciences*, 108(30):12233–12237, 2011.
- [5] Hyobin Yoo, Rebecca Engelke, Stephen Carr, Shiang Fang, Kuan Zhang, Paul Cazeaux, Suk Hyun Sung, Robert Hovden, Adam W. Tsen, Takashi Taniguchi, Kenji Watanabe, Gyu-Chul Yi, Miyoung Kim, Mitchell Luskin, Ellad B. Tadmor, Efthimios Kaxiras, and Philip Kim. Atomic and electronic reconstruction at van der Waals interface in twisted bilayer graphene. *Nature Materials*, pages 448–453, 2019.
- [6] Stephen Carr, Daniel Massatt, Shiang Fang, Paul Cazeaux, Mitchell Luskin, and Efthimios Kaxiras. Twistrionics: manipulating the electronic properties of two-dimensional layered structures through the twist angle. *Phys. Rev. B*, 95:075420, 2017.
- [7] Xipeng Wang, Simón Ramírez-Hinestrosa, Jure Dobnikar, and Daan Frenkel. The Lennard-Jones potential: when (not) to use it. *Physical Chemistry Chemical Physics*, 22(19):10624–10633, 2020.
- [8] Murray S Daw, Stephen M Foiles, and Michael I Baskes. The embedded-atom method: a review of theory and applications. *Materials Science Reports*, 9(7-8):251–310, 1993.
- [9] RLC Vink, GT Barkema, WF Van der Weg, and Normand Mousseau. Fitting the Stillinger–Weber potential to amorphous silicon. *Journal of non-crystalline solids*, 282(2-3):248–255, 2001.
- [10] Aleksey N. Kolmogorov and Vincent H. Crespi. Registry-dependent interlayer potential for graphitic systems. *Phys. Rev. B*, 71:235415, Jun 2005.
- [11] Noa Marom, Jonathan Bernstein, Jonathan Garel, Alexandre Tkatchenko, Ernesto Joselevich, Leeor Kronik, and Oded Hod. Stacking and registry effects in layered materials: The case of hexagonal boron nitride. *Phys. Rev. Lett.*, 105:046801, Jul 2010.
- [12] Jörg Behler and Michele Parrinello. Generalized neural-network representation of high-dimensional potential-energy surfaces. *Phys. Rev. Lett.*, 98:146401, Apr 2007.
- [13] Albert P Bartók, Mike C Payne, Risi Kondor, and Gábor Csányi. Gaussian approximation potentials: The accuracy of quantum mechanics, without the electrons. *Physical review letters*, 104(13):136403, 2010.
- [14] A.P. Thompson, L.P. Swiler, C.R. Trott, S.M. Foiles, and G.J. Tucker. Spectral neighbor analysis method for automated generation of quantum-accurate interatomic potentials. *Journal of Computational Physics*, 285:316–330, 2015.
- [15] Alexander V. Shapeev. Moment tensor potentials: A class of systematically improvable interatomic potentials. *Multiscale Modeling & Simulation*, 14(3):1153–1173, 2016.
- [16] Ralf Drautz. Atomic cluster expansion for accurate and transferable interatomic potentials. *Phys. Rev. B*, 99:014104, Jan 2019.
- [17] Volker L. Deringer, Miguel A. Caro, and Gábor Csányi. Machine learning interatomic potentials as emerging tools for materials science. *Advanced Materials*, 31(46):1902765, 2019.
- [18] Jörg Behler and Gábor Csányi. Machine learning potentials for extended systems: a perspective. *The European Physical Journal B*, 94, 2021.
- [19] Volker L. Deringer, Albert P. Bartók, Noam Bernstein, David M. Wilkins, Michele Ceriotti, and Gábor Csányi. Gaussian process regression for materials and molecules. *Chemical Reviews*, 121(16):10073–10141, 2021. PMID: 34398616.
- [20] Felix Musil, Andrea Grisafi, Albert P. Bartók, Christoph Ortner, Gábor Csányi, and Michele Ceriotti. Physics-inspired structural representations for molecules and materials. *Chemical Reviews*, 121(16):9759–9815, 2021. PMID: 34310133.
- [21] Atsuto Seko, Atsushi Togo, and Isao Tanaka. Group-theoretical high-order rotational invariants for structural representations: Application to linearized machine learning interatomic potential. *Physical Review B*, 99, 06 2019.
- [22] Geneviève Dussan, Markus Bachmayr, Gábor Csányi, Ralf Drautz, Simon Etter, Cas van der Oord, and Christoph Ortner.

- Atomic cluster expansion: Completeness, efficiency and stability. *Journal of Computational Physics*, 454:110946, 2022.
- [23] Yury Lysogorskiy, Cas van der Oord, Anton Bochkarev, Sarath Menon, Matteo Rinaldi, Thomas Hammerschmidt, Matous Mrovec, Aidan Thompson, Gábor Csányi, Christoph Ortner, and Ralf Drautz. Performant implementation of the atomic cluster expansion (pace) and application to copper and silicon. *npj Computational Materials*, 7(1):97, 2021.
- [24] Dávid Péter Kovács, Cas van der Oord, Jiri Kucera, Alice E. A. Allen, Daniel J. Cole, Christoph Ortner, and Gábor Csányi. Linear atomic cluster expansion force fields for organic molecules: Beyond RMSE. *Journal of Chemical Theory and Computation*, 17(12):7696–7711, 2021. PMID: 34735161.
- [25] Cas Oord, Matthias Sachs, David Kovacs, Christoph Ortner, and Gábor Csányi. Hyperactive learning for data-driven interatomic potentials. *npj Computational Materials*, 9, 09 2023.
- [26] Y. Liang, M. Mrovec, Y. Lysogorskiy, M. Vega-Paredes, C. Scheu, and R. Drautz. Atomic cluster expansion for Pt-Rh catalysts: From ab initio to the simulation of nanoclusters in few steps. arXiv:2303.07465.
- [27] Anton Bochkarev, Yury Lysogorskiy, Sarath Menon, Minaam Qamar, Matous Mrovec, and Ralf Drautz. Efficient parametrization of the atomic cluster expansion. *Phys. Rev. Mater.*, 6:013804, 2022.
- [28] M. Qamar, M. Mrovec, Y. Lysogorskiy, A. Bochkarev, and R. Drautz. Atomic cluster expansion for quantum-accurate large-scale simulations of carbon. arXiv:2210.09161.
- [29] Bohayra Mortazavi, Ivan S Novikov, Evgeny V Podryabinkin, Stephan Roche, Timon Rabczuk, Alexander V Shapeev, and Xiaoying Zhuang. Exploring phononic properties of two-dimensional materials using machine learning interatomic potentials. *Applied Materials Today*, 20:100685, 2020.
- [30] Bohayra Mortazavi, Evgeny V Podryabinkin, Ivan S Novikov, Stephan Roche, Timon Rabczuk, Xiaoying Zhuang, and Alexander V Shapeev. Efficient machine-learning based interatomic potentials for exploring thermal conductivity in two-dimensional materials. *Journal of Physics: Materials*, 3(2):02LT02, 2020.
- [31] Juan M Marmolejo-Tejada and Martín A Mosquera. Thermal properties of single-layer MoS<sub>2</sub>-WS<sub>2</sub> alloys enabled by machine-learned interatomic potentials. *Chemical Communications*, 58(49):6902–6905, 2022.
- [32] Tuğbey Kocabaş, Murat Keçeli, Álvaro Vázquez-Mayagoitia, and Cem Sevik. Gaussian approximation potentials for accurate thermal properties of two-dimensional materials. *Nanoscale*, 15(19):8772–8780, 2023.
- [33] Anas Siddiqui and Nicholas D. M. Hine. Machine-learned interatomic potentials for transition metal dichalcogenide mo<sub>1-x</sub>w<sub>x</sub>s<sub>2</sub>-y<sub>se</sub><sub>2</sub>y alloys. *npj Computational Materials*, 2024.
- [34] Samuel J Magorrian, Anas Siddiqui, and Nicholas DM Hine. Strong atomic reconstruction in twisted bilayers of highly flexible in<sub>se</sub>: Machine-learned interatomic potential and continuum model approaches. *arXiv preprint arXiv:2406.19462*, 2024.
- [35] Gang Seob Jung, Hunjoo Myung, and Stephan Irle. Artificial neural network potentials for mechanics and fracture dynamics of two-dimensional crystals. *Machine Learning: Science and Technology*, 4(3):035001, 2023.
- [36] Haoyu Yin, Muzi Xu, Zhiyao Luo, Xiaotian Bi, Jiali Li, Sui Zhang, and Xiaonan Wang. Machine learning for membrane design and discovery. *Green Energy & Environment*, 9(1):54–70, 2024.
- [37] Nathan Wilson, Daniel Willhelm, Xiaoning Qian, Raymundo Arróyave, and Xiaofeng Qian. Batch active learning for accelerating the development of interatomic potentials. *Computational Materials Science*, 208:111330, 2022.
- [38] Ting Bao, Ning Mao, Wenhui Duan, Yong Xu, Adrian Del Maestro, and Yang Zhang. Transfer learning electronic structure: millielectron volt accuracy for sub-million-atom moiré semiconductor. *arXiv preprint arXiv:2501.12452*, 2025.
- [39] Jiaxuan Liu, Zhong Fang, Hongming Weng, and Quansheng Wu. Dpmoire: A tool for constructing accurate machine learning force fields in moiré systems, 2024.
- [40] Johnathan D Georganas, Akash Ramdas, Chung Hsuan Shan, Elena Halsted, Tianshu Li, Felipe H da Jornada, et al. Accurate, transferable, and verifiable machine-learned interatomic potentials for layered materials. *arXiv preprint arXiv:2503.15432*, 2025.
- [41] Georgios A. Tritsarlis, Sharmila N. Shirodkar, Efthimios Kaxiras, Paul Cazeaux, Mitchell Luskin, Petr Plecháč, and Eric Cancès. Perturbation theory for weakly coupled two-dimensional layers. *Journal of Materials Research*, 31:959–966, 4 2016.
- [42] Stephen Carr, Shiang Fang, and Efthimios Kaxiras. Electronic-structure methods for twisted moiré layers. *Nature Reviews Materials*, 5(10):748–763, July 2020.
- [43] Daniel Massatt, Mitchell Luskin, and Christoph Ortner. Electronic density of states for incommensurate layers. *Multiscale Model. Simul.*, 15:476–499, 2017.
- [44] Paul Cazeaux, Mitchell Luskin, and Daniel Massatt. Energy minimization of two dimensional incommensurate heterostructures. *Archive for Rational Mechanics and Analysis*, 235(2):1289–1325, aug 2019.
- [45] S. Carr, D. Massatt, S. B. Torrisi, P. Cazeaux, M. Luskin, and E. Kaxiras. Relaxation and Domain Formation in Incommensurate 2D Heterostructures. *Phys. Rev. B*, page 224102 (7 pp), 2018.
- [46] Ziyang Zhu, Stephen Carr, Daniel Massatt, Mitchell Luskin, and Efthimios Kaxiras. Twisted trilayer graphene: A precisely tunable platform for correlated electrons. *Phys. Rev. Lett.*, 125:11604 (6 pp), 2020.
- [47] Ziyang Zhu, Paul Cazeaux, Mitchell Luskin, and Efthimios Kaxiras. Modeling mechanical relaxation in incommensurate trilayer van der Waals heterostructures. *Phys. Rev. B*, page 224107 (14 pp), 2020.
- [48] Yuan Cao, Vida Fatemi, Shiang Fang, Kenji Watanabe, Takashi Taniguchi, Efthimios Kaxiras, and Pablo Jarillo-Herrero. Unconventional superconductivity in magic-angle graphene superlattices. *Nature*, 556(7699):43–50, 2018.
- [49] Heonjoon Park, Jiaqi Cai, Eric Anderson, Yinong Zhang, Jiayi Zhu, Xiaoyu Liu, Chong Wang, William Holtzmann, Chaowei Hu, Zhaoyu Liu, Takashi Taniguchi, Kenji Watanabe, Jiun-Haw Chu, Ting Cao, Liang Fu, Wang Yao, Cui-Zu Chang, David Cobden, Di Xiao, and Xiaodong Xu. Observation of fractionally quantized anomalous hall effect. *Nature*, 622(7981):74–79, 2023.

- [50] Jiaqi Cai, Eric Anderson, Chong Wang, Xiaowei Zhang, Xiaoyu Liu, William Holtzmann, Yinong Zhang, Fengren Fan, Takashi Taniguchi, Kenji Watanabe, Ying Ran, Ting Cao, Liang Fu, Di Xiao, Wang Yao, and Xiaodong Xu. Signatures of fractional quantum anomalous hall states in twisted mote2. *Nature*, 622(7981):63–68, 2023.
- [51] Paul Cazeaux, Drake Clark, Rebecca Engelke, Philip Kim, and Mitchell Luskin. Relaxation and domain wall structure of bilayer moiré systems. *Journal of Elasticity*, pages 1–24, 04 2023.
- [52] Shuyang Dai, Yang Xiang, and David J Srolovitz. Twisted bilayer graphene: Moiré with a twist. *Nano letters*, 16(9):5923–5927, 2016.
- [53] Nguyen N. T. Nam and Mikito Koshino. Lattice relaxation and energy band modulation in twisted bilayer graphene. *Phys. Rev. B*, 96:075311, Aug 2017.
- [54] Kejie Fu, Mingjie Liao, Yangshuai Wang, Jianjun Chen, and Lei Zhang. Adaptive multigrid strategy for geometry optimization of large-scale three dimensional molecular mechanics. *Journal of Computational Physics*, 485:112113, 2023.
- [55] Mikito Koshino and Young-Woo Son. Moiré phonons in twisted bilayer graphene. *Phys. Rev. B*, 100:075416, Aug 2019.
- [56] Jonathan Z. Lu, Ziyang Zhu, Mattia Angeli, Daniel T. Larson, and Efthimios Kaxiras. Low-energy moiré phonons in twisted bilayer van der waals heterostructures. *Phys. Rev. B*, 106:144305, Oct 2022.
- [57] Michael Hott, Alexander B. Watson, and Mitchell Luskin. From incommensurate bilayer heterostructures to allen-cahn: An exact thermodynamic limit. *Arch. Rat. Mech. Anal.*, to appear.
- [58] Julian Braun, Christoph Ortner, Yangshuai Wang, and Lei Zhang. Higher-order far-field boundary conditions for crystalline defects. *SIAM Journal on Numerical Analysis*, 63(2):520–541, 2025.
- [59] Derek Olson, Christoph Ortner, Yangshuai Wang, and Lei Zhang. Elastic far-field decay from dislocations in multilattices. *Multiscale Modeling & Simulation*, 21(4):1379–1409, 2023.
- [60] Hyobin Yoo, Rebecca Engelke, Stephen Carr, Shiang Fang, Kuan Zhang, Paul Cazeaux, Suk Hyun Sung, Robert Hovden, Adam W. Tsen, Takashi Taniguchi, Kenji Watanabe, Gyu-Chul Yi, Miyoung Kim, Mitchell Luskin, Ellad B. Tadmor, Efthimios Kaxiras, and Philip Kim. Atomic and electronic reconstruction at the van der waals interface in twisted bilayer graphene. *Nature Materials*, 18(5):448–453, 2019.
- [61] John Birkbeck, Jiewen Xiao, Alon Inbar, Takashi Taniguchi, Kenji Watanabe, Erez Berg, Leonid Glazman, Francisco Guinea, Felix von Oppen, and Shahal Ilani. Measuring phonon dispersion and electron-phason coupling in twisted bilayer graphene with a cryogenic quantum twisting microscope. *arXiv preprint arXiv:2407.13404*, 2024.
- [62] M M van Wijk, A Schuring, M I Katsnelson, and A Fasolino. Relaxation of moiré patterns for slightly misaligned identical lattices: graphene on graphite. *2D Materials*, 2(3):034010, July 2015.
- [63] Mingjian Wen, Stephen Carr, Shiang Fang, Efthimios Kaxiras, and Ellad B. Tadmor. Dihedral-angle-corrected registry-dependent interlayer potential for multilayer graphene structures. *Phys. Rev. B*, 98:235404, Dec 2018.
- [64] W. C. Witt, C. van der Oord, E. Gelžinytė, T. Järvinen, A. Ross, J. P. Darby, C. H. Ho, W. J. Baldwin, M. Sachs, J. Kermodé, N. Bernstein, G. Csányi, and C. Ortner. Acepotentials.jl: A Julia implementation of the atomic cluster expansion. *J. Chem. Phys.*, 159:164101, 2023.
- [65] Stefan Grimme, Jens Antony, Stephan Ehrlich, and Helge Krieg. A consistent and accurate ab initio parametrization of density functional dispersion correction (DFT-D) for the 94 elements H-Pu. *The Journal of Chemical Physics*, 132(15):154104, 2010.
- [66] Ilyes Batatia, Philipp Benner, Yuan Chiang, Alin M. Elena, Dávid P. Kovács, and Janosh Riebesell et al. A foundation model for atomistic materials chemistry. *ArXiv e-prints*, 2401.00096, 2024. (62 authors not shown).
- [67] Jie Ma, Dario Alfè, Angelos Michaelides, and Enge Wang. Stone-Wales defects in graphene and other planar sp 2-bonded materials. *Physical Review B—Condensed Matter and Materials Physics*, 80(3):033407, 2009.
- [68] Akhil Shajan, Madushanka Manathunga, Andreas W Gotz, and Kenneth M Merz Jr. Geometry optimization: A comparison of different open-source geometry optimizers. *Journal of Chemical Theory and Computation*, 19(21):7533–7541, 2023.
- [69] Hannes Jónsson, Greg Mills, and Karsten W Jacobsen. Nudged elastic band method for finding minimum energy paths of transitions. In *Classical and quantum dynamics in condensed phase simulations*, pages 385–404. World Scientific, 1998.
- [70] Dong C Liu and Jorge Nocedal. On the limited memory bfgs method for large scale optimization. *Mathematical programming*, 45(1):503–528, 1989.
- [71] CR Wilke and Pin Chang. Correlation of diffusion coefficients in dilute solutions. *AIChE journal*, 1(2):264–270, 1955.
- [72] Cheng Shen, Yanbang Chu, QuanSheng Wu, Na Li, Shuopei Wang, Yanchong Zhao, Jian Tang, Jieying Liu, Jinpeng Tian, Kenji Watanabe, et al. Correlated states in twisted double bilayer graphene. *Nature Physics*, 16(5):520–525, 2020.
- [73] Albert Einstein. *Investigations on the Theory of the Brownian Movement*. Courier Corporation, 1956.
- [74] Pedro Alcázar Guerrero, Viet-Hung Nguyen, Aron W Cummings, José-Hugo Garcia, Jean-Christophe Charlier, and Stephan Roche. Disorder-induced delocalization in magic-angle twisted bilayer graphene. *arXiv preprint arXiv:2401.08265*, 2024.
- [75] Yajuan Cheng, Zheyong Fan, Tao Zhang, Masahiro Nomura, Sebastian Volz, Guimei Zhu, Baowen Li, and Shiyun Xiong. Magic angle in thermal conductivity of twisted bilayer graphene. *Materials Today Physics*, 35:101093, 2023.
- [76] Matthew Yankowitz, Shaowen Chen, Hryhorii Polshyn, Yuxuan Zhang, Kenji Watanabe, Takashi Taniguchi, David Graf, Andrea F Young, and Cory R Dean. Tuning superconductivity in twisted bilayer graphene. *Science*, 363(6431):1059–1064, 2019.
- [77] Philip Kim and Matthew Yankowitz. Van der waals heterostructures. *Nature*, 544(7649):19–23, 2016.
- [78] Christian Carbogno, Rampi Ramprasad, and Matthias Scheffler. Ab initio green-kubo approach for the thermal conductivity of solids. *Physical review letters*, 118(17):175901, 2017.
- [79] Ferry Faizal, I Joni, et al. Thermal transport in twisted bilayer graphene: An equilibrium molecular dynamics study. *arXiv preprint arXiv:2212.10216*, 2022.
- [80] Hongyang Li, Hao Ying, Xiangping Chen, Denis L Nika, Alexandr I Cocemasov, Weiwei Cai, Alexander A Balandin, and

- Shanshan Chen. Thermal conductivity of twisted bilayer graphene. *Nanoscale*, 6(22):13402–13408, 2014.
- [81] Jonathan Z. Lu, Ziyang Zhu, Mattia Angeli, Daniel T. Larson, and Efthimios Kaxiras. Low-energy moiré phonons in twisted bilayer van der waals heterostructures. *Phys. Rev. B*, 106:144305, Oct 2022.
- [82] A. Uri, S. Grover, Y. Cao, J. A. Crosse, K. Bagani, D. Rodan-Legrain, Y. Myasoedov, K. Watanabe, T. Taniguchi, P. Moon, M. Koshino, P. Jarillo-Herrero, and E. Zeldov. Mapping the twist-angle disorder and landau levels in magic-angle graphene. *Nature*, 581(7806):47–52, 2020.
- [83] Nathanael P. Kazmierczak, Madeline Van Winkle, Colin Ophus, Karen C. Bustillo, Stephen Carr, Hamish G. Brown, Jim Ciston, Takashi Taniguchi, Kenji Watanabe, and D. Kwabena Bediako. Strain fields in twisted bilayer graphene. *Nature Materials*, 20(7):956–963, 2021.
- [84] Yangshuai Wang, Shashwat Patel, and Christoph Ortner. A theoretical case study of the generalization of machine-learned potentials. *Computer Methods in Applied Mechanics and Engineering*, 422:116831, 2024.
- [85] H. Chen, C. Ortner, and Y. Wang. QM/MM methods for crystalline defects. part 3: machine-learned mm models. *Multiscale Model. Simul.*, 20(4):1490–1518, 2022.
- [86] C. Ortner and Y. Wang. A framework for a generalization analysis of machine-learned interatomic potentials. *Multiscale Model. Simul.*, 21(3):1053–1080, 2023.
- [87] Tina Torabi, Christoph Ortner, and Yangshuai Wang. Surrogate models for vibrational entropy based on a spatial decomposition. *Multiscale Modeling & Simulation*, 23(1):514–544, 2025.
- [88] M. Bachmayr, G. Dussan, C. Ortner, and J. Thomas. Polynomial approximation of symmetric functions. *Math. Comp.*, 93:811–839, 2024.
- [89] A. Bochkarev, Y. Lysogorskiy, C. Ortner, G. Csanyi, and R. Drautz. Multilayer atomic cluster expansion for semi-local interactions. *Phys. Rev. Research*, 4, 2022.
- [90] S. Das, P. Motamarri, V. Subramanian, D. M. Rogers, and V. Gavini. DFT-FE 1.0: A massively parallel hybrid cpu-gpu density functional theory code using finite-element discretization. *Computer Physics Communications*, 280:108473, 2022.
- [91] P. Motamarri, S. Das, S. Rudraraju, K. Ghosh, D. Davydov, and V. Gavini. DFT-FE – A massively parallel adaptive finite-element code for large-scale density functional theory calculations. *Computer Physics Communications*, 246:106853, 2020.
- [92] P. Motamarri and V. Gavini. Configurational forces in electronic structure calculations using Kohn-Sham density functional theory. *Phys. Rev. B*, 97:165132, Apr 2018.
- [93] P. Motamarri, M.R. Nowak, K. Leiter, J. Knap, and V. Gavini. Higher-order adaptive finite-element methods for Kohn–Sham density functional theory. *Journal of Computational Physics*, 253:308–343, 2013.
- [94] Yunkai Zhou, Yousef Saad, Murilo L. Tiago, and James R. Chelikowsky. Parallel self-consistent-field calculations via chebyshev-filtered subspace acceleration. *Phys. Rev. E*, 74:066704, Dec 2006.
- [95] Sambit Das, Phani Motamarri, Vikram Gavini, Bruno Turcksin, Ying-Wai Li, and Brent Leback. Fast, scalable and accurate finite-element based ab initio calculations using mixed precision computing: 46 pflops simulation of a metallic dislocation system. In *Proceedings of the International Conference for High Performance Computing, Networking, Storage and Analysis*, pages 1–12, 2019.
- [96] Sambit Das, Bikash Kanungo, Vishal Subramanian, Gourab Panigrahi, Phani Motamarri, David Rogers, Paul Zimmerman, and Vikram Gavini. Large-scale materials modeling at quantum accuracy: Ab initio simulations of quasicrystals and interacting extended defects in metallic alloys. In *Proceedings of the International Conference for High Performance Computing, Networking, Storage and Analysis*, pages 1–12, 2023.
- [97] D. R. Hamann. Optimized norm-conserving Vanderbilt pseudopotentials. *Phys. Rev. B*, 88:239906, 1995.
- [98] Mostafa Faghieh Shojaei, John E. Pask, Andrew J. Medford, and Phanish Suryanarayana. Soft and transferable pseudopotentials from multi-objective optimization. *Computer Physics Communications*, 283:108594, 2023.